

Spin resonance without spin splitting

M. Hell,^{1,2} B. Sothmann,³ M. Leijnse,⁴ M. R. Wegewijs,^{1,2,5} and J. König⁶

¹*Peter Grünberg Institut, Forschungszentrum Jülich, 52425 Jülich, Germany*

²*JARA-Fundamentals of Future Information Technology, Forschungszentrum Jülich, 52425 Jülich, Germany*

³*Département de Physique Théorique, Université de Genève, CH-1211 Genève 4, Switzerland*

⁴*Solid State Physics and Nanometer Structure Consortium (nmC@LU), Lund University, 221 00 Lund, Sweden*

⁵*Institute for Theory of Statistical Physics, RWTH Aachen, 52056 Aachen, Germany*

⁶*Theoretische Physik and CENIDE, Universität Duisburg-Essen, 47048 Duisburg, Germany*

(Received 17 March 2014; revised manuscript received 2 February 2015; published 6 May 2015)

We predict that a single-level quantum dot without discernible splitting of its spin states develops a spin-precession resonance in charge transport when embedded into a spin valve. The resonance occurs in the generic situation of Coulomb blockaded transport with ferromagnetic leads whose polarizations deviate from perfect antiparallel alignment. The resonance appears when electrically tuning the interaction-induced exchange field perpendicular to one of the polarizations—a simple condition relying on vectors in contrast to usual resonance conditions associated with energy splittings. The spin resonance can be detected by stationary dI/dV spectroscopy and by oscillations in the time-averaged current using a gate-pulsing scheme. The generic noncollinearity of the ferromagnets and junction asymmetry allow for an all-electric determination of the spin-injection asymmetry, the anisotropy of spin relaxation, and the magnitude of the exchange field. We also investigate the impact of a nearby superconductor on the resonance position. Our simplistic model turns out to be generic for a broad class of coherent few-level quantum systems.

DOI: [10.1103/PhysRevB.91.195404](https://doi.org/10.1103/PhysRevB.91.195404)

PACS number(s): 85.75.-d, 73.63.Kv, 85.35.-p

I. INTRODUCTION

Gaining fast, coherent control over a few spins or even a single spin is at the heart of current experimental efforts in both spintronics [1–3] and solid-state quantum computing [4–7]. Single-molecule magnets in gateable nanojunctions [8–11] or adatoms and molecules manipulated by STM [1,12–14] provide a bottom-up approach to achieve this goal. Promising top-down routes combine conventional spin valves [15–19] with nanoscale quantum dot (QD) devices [20–26]. Such coherent quantum systems are typically manipulated through resonance techniques, e.g., by electromagnetic pulses [5,6]. In general, this requires that the frequency of the applied pulses matches the splitting of, e.g., a two-level system. In this paper we predict that quite generically resonances can appear in systems with quasidegenerate levels that do not involve such a matching to a splitting. Instead, a condition involving *vectors* has to be satisfied.

We illustrate this for a QD embedded in a noncollinear spin valve, a specific example relevant for spintronics and spin-based quantum computation. It leads to an unexpected, strongly gate-voltage dependent feature in the stationary nonlinear conductance (dI/dV_b) extending all across the Coulomb blockade regime. It arises under nonequilibrium conditions but disappears upon reversing the bias voltage. Strikingly, it can appear at voltages much larger or smaller than any of the naively expected energy scales, showing that it does not fit into the usual classification of resonances. All these features distinguish this resonance from known effects in the Coulomb blockade regime [24,27,28], including those due to inelastic cotunneling resolving excitations [29–31], the Kondo effect [32–35], and another zero-bias anomaly specific to QD spin valves [24,28].

The anomalous resonance we predict here relies on the coherent precession of a single spin that is driven by the

Coulomb interaction-induced *exchange field* [35–41]. The exchange field is a generic renormalization effect [31,42–45] arising from quantum fluctuations of QD electrons into the attached ferromagnets. This leads to a spin-dependent level shift, i.e., an effective magnetic field, because the tunneling rates into the ferromagnets are spin dependent. While this exchange field has been measured for strong tunnel coupling Γ as an induced level splitting for collinear polarizations [32–35], the sharp resonance that we predict here appears for moderate tunnel couplings when this splitting *cannot* be resolved. In this case, the exchange field can still have an impact under the additional requirement that the rotational symmetry is broken completely by a noncollinear magnetic configuration of the spin valve. Here each ferromagnet induces a contribution to the exchange field along its polarization, which strongly depends on the applied voltages. This adds a tunable component to the exchange field that is perpendicular to the injected spins. This induces a spin precession that results in measurable consequences for the stationary conductance [36,40,46] and the noise spectrum [47,48], also for hybrid setups with a superconductor [49].

However, the features discussed so far change on large voltage scales in contrast to the sharp resonance presented in this work. This relates to the limitation of these prior works to the sequential tunneling regime where the electron dwell times $1/\Gamma$ are too small for single spins to precess by a large angle. To find a sharp resonance one needs a suppression of the spin decoherence, which is achieved in our case by an exponentially small leading-order Γ contribution due to the Coulomb interaction U . Our spin resonance thus appears in the Coulomb blockade regime of a QD spin valve where the spin decoherence is limited by higher-order contributions $\propto \Gamma^2/U$, while the spin-precession period is still dominated by the leading-order Γ exchange field [50].

Only a few studies address spin-precession effects in the Coulomb-blockade regime [50,51]. What has been overlooked in those works is that a simple QD spin valve already has built-in capabilities for single-spin operations through the gate-voltage control over the exchange field *direction* in the fixed, nearly antiparallel configuration. We show that the resulting spin resonance can be exploited in a gate-pulsing scheme to provide single-spin control for quantum-gate operations. Time-averaged current measurements directly probe the underdamped spin precession.

The paper is organized as follows: In Sec. II we first introduce the QD spin-valve model under consideration and discuss our quantum master equation approach to describe the dynamics of the QD system. Based on the solution of these equations, we compute the stationary conductance that exhibits the above-mentioned spin resonance. We substantiate the simple resonance condition in Sec. III and identify relevant parameter combinations that characterize the resonance features (position and width). We further suggest procedures to extract these parameters from experimental data in order to characterize QD spin valves. Next, we propose in Sec. IV a simple gate-pulsing scheme, which is shown to reveal the underdamped spin precession occurring near the spin resonance. Finally, we summarize our findings in Sec. V and argue that the resonance mechanism described here is generic for a broad class of coherently evolving quantum systems renormalized through their environment.

II. MODEL AND KINETIC EQUATIONS

The spin resonance appears in the simplest QD spin-valve model one can think of, which is introduced in Sec. II A. This is remarkable since this model of an interacting, single, spin-degenerate orbital level, which is tunnel coupled to two noncollinearly polarized ferromagnetic leads, has been studied quite intensively. In Sec. II B we discuss the quantum master equation for the QD density operator ρ , which is required to address this spintronic effect. Based on the solution of these equations, we derive the current that exhibits the spin-resonance feature.

A. Complete breaking of rotational symmetry in quantum-dot spin valves

The system under study, see Fig. 1, consists of a QD, which is tunnel coupled to two ferromagnetic leads r , labeled with $r = s(\text{ource}), d(\text{rain})$. The Hamiltonian reads

$$H_{\text{tot}} = H + \sum_{r=s,d} H_r + H_T. \quad (1)$$

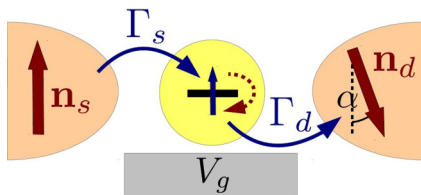


FIG. 1. (Color online) Schematic setup of a QD spin valve, indicating the spin-precession resonance mechanism.

The QD is modeled by a single, spin-degenerate, interacting orbital level,

$$H = \sum_{\sigma} \epsilon d_{\sigma}^{\dagger} d_{\sigma} + U d_{\uparrow}^{\dagger} d_{\uparrow} d_{\downarrow}^{\dagger} d_{\downarrow}, \quad (2)$$

where d_{σ}^{\dagger} (d_{σ}) are fermionic field operators that create (annihilate) electrons with spin σ in the QD. The QD Hamiltonian (2) is spin *isotropic*, that is,

$$[H, \hat{S}_i] = 0, \quad (3)$$

where

$$\hat{S}_i = \sum_{\sigma\sigma'} \frac{1}{2} (\sigma_i)_{\sigma\sigma'} d_{\sigma}^{\dagger} d_{\sigma'}, \quad (4)$$

is the i th Cartesian component ($i = x, y, z$) of the spin vector operator and the σ_i denote the Pauli matrices. The spin isotropy of the QD model implies that the two spin states are degenerate.

By contrast, the spin symmetry is broken in the ferromagnets, held at equal temperature T and different electrochemical potentials $\mu_{s(d)} = \pm V_b/2$, with Hamiltonian

$$H_r = \sum_{k\sigma} \epsilon_{rk\sigma} c_{rk\sigma}^{\dagger} c_{rk\sigma}, \quad (5)$$

where $c_{rk\sigma}^{\dagger}$ ($c_{rk\sigma}$) are fermionic field operators that create (annihilate) electrons in single-particle states $|rk\sigma\rangle = |rk\rangle \otimes |\sigma\rangle_r = c_{rk\sigma}^{\dagger} |0\rangle$ of lead r . The spin-quantization axis is chosen for each ferromagnet along its polarization vector \mathbf{n}_r . The spin-dependent band structure of the ferromagnets is described by the spin-dependent density of states (DOS), here limiting ourselves to a flat band with

$$v_{r\sigma}(\omega) = \sum_k \delta(\omega - \epsilon_{rk\sigma}) = \bar{v}_r (1 + \sigma n_r), \quad (6)$$

for $|\omega| < W$ (half-bandwidth) and zero otherwise. In Eq. (6) we introduced the spin-averaged DOS $\bar{v}_r = (v_{r,\uparrow} + v_{r,\downarrow})/2$ and the polarization $n_r = |\mathbf{n}_r| = (v_{r,\uparrow} - v_{r,\downarrow})/(v_{r,\uparrow} + v_{r,\downarrow})$, which do not depend on the frequency ω .

The breaking of the spin symmetry in the ferromagnets is expressed by

$$[H_r, \hat{\mathbf{n}}_{r,\perp} \cdot \hat{\mathbf{S}}_r] \neq 0. \quad (7)$$

Here $\hat{\mathbf{n}}_{r,\perp} \cdot \hat{\mathbf{S}}_r$ is a component of the spin operator $\hat{\mathbf{S}}_r = \sum_{k\sigma\sigma'} \langle \sigma | \hat{\mathbf{S}} | \sigma' \rangle_r c_{rk\sigma}^{\dagger} c_{rk\sigma'}$ of ferromagnet r along a unit vector $\hat{\mathbf{n}}_{r,\perp}$ that is perpendicular to $\hat{\mathbf{n}}_r$. Note that for each ferromagnet, the axial symmetry along its spontaneous magnetization direction, given by $\hat{\mathbf{n}}_r$, remains intact: $[H_r, \hat{\mathbf{n}}_r \cdot \hat{\mathbf{S}}_r] = 0$. Importantly, the spin resonance relies on a *complete* breaking of the spin symmetry by the ferromagnets, which means the full Hamiltonian does not commute with *any* component $i = x, y, z$ of the total spin operator $\hat{\mathbf{S}}_{\text{tot}} = \hat{\mathbf{S}} + \sum_r \hat{\mathbf{S}}_r$, that is,

$$[H, \hat{S}_{\text{tot},i}] \neq 0. \quad (8)$$

This is achieved for noncollinearly polarized ferromagnets with polarizations \mathbf{n}_s and \mathbf{n}_d at an angle $\theta = \pi - \alpha \neq 0, \pi$. Finally, the tunnel coupling Hamiltonian reads

$$H_T = \sum_{rk\sigma} t_{r,\sigma\sigma'} d_{\sigma}^{\dagger} c_{rk\sigma'} + \text{H.c.} \quad (9)$$

Here the tunneling amplitudes are assumed to be k and therefore energy independent as well as spin *conserving*, that is,

$$[H_T, \hat{S}_{\text{tot}}] = 0. \quad (10)$$

However, since d_{σ}^{\dagger} and $c_{rk\sigma}$ may refer to different spin quantization axes, the tunneling amplitudes

$$t_{r,\sigma\sigma'} = \langle \sigma | \sigma' \rangle_r t_r \quad (11)$$

incorporate an overlap factor of the spin states while the bare tunneling amplitudes t_r are spin *independent*. They set the spin-averaged tunneling rates by $\Gamma_r = 2\pi \bar{v}_r |t_r|^2$.

B. Kinetic equations and charge current for infinite interaction energy

The transport signatures of the QD spin valve are governed by the nonequilibrium dynamics on the QD, described by its reduced density operator $\rho = \text{Tr}_{\text{res}}(\rho_{\text{tot}})$. Our reduced density operator approach starts, as usual, from the von Neumann equation $\dot{\rho}_{\text{tot}} = -i[H, \rho_{\text{tot}}]$ for the density operator of the full system ρ_{tot} . Eliminating the reservoir degrees of freedom results in the following kinetic equation for the reduced density operator of the QD:

$$\dot{\rho}(t) = -i[H, \rho(t)] + W\rho(t). \quad (12)$$

Here we have made an additional Markov approximation since we are interested either in the stationary current obtained from the stationary state satisfying $\dot{\rho}_{\text{st}} = 0$ (for which it is irrelevant) or the time-dependent current for which non-Markovian corrections are of subordinate importance in our case as discussed in Appendix B 5. Thus, the effects due to the coupling to the leads are incorporated through the zero-frequency kernel W .

To facilitate the analytical discussion of the QD spin dynamics, we express Eq. (12) in terms of coupled equations for the occupation probabilities p_n for each of the charge states $n = 0, 1, 2$, and the average spin $\mathbf{S} = \text{Tr}_{\text{QD}}(\hat{\mathbf{S}}\rho)$. The equivalence of these two representations is shown in Appendix A. To keep all analytic expressions as simple as possible, we focus first on the limit of $U \rightarrow \infty$, for which double occupancy of the QD is suppressed (which implies $p_2 = 0$). In this case, the kinetic equations read

$$\begin{aligned} \dot{p}_0 &= -2\Gamma_0 p_0 + \Gamma_1 p_1 + 2\mathbf{G}_{pS} \cdot \mathbf{S}, \\ \dot{\mathbf{S}} &= +\mathbf{G}_{Sp}^0 p_0 - \frac{1}{2}\mathbf{G}_{Sp}^1 p_1 - \mathcal{R}_S \cdot \mathbf{S} - \mathbf{B} \times \mathbf{S}, \end{aligned} \quad (13)$$

with $\dot{p}_0 = -\dot{p}_1$ due to probability conservation: $p_0 + p_1 = 1$. Equation (13) is the most general form of any time-local quantum master equation for the QD system we study. It extends common master equation approaches for the occupation probabilities p_n by including their intense coupling (through the vectors $\mathbf{G}_{Sp}^0, \mathbf{G}_{Sp}^1, \mathbf{G}_{pS}$) to the coherences [52,53] of the degenerate spin states, contained in the spin vector \mathbf{S} . Furthermore, the spin is subject to a torque corresponding to an effective exchange field \mathbf{B} . This effective field arises from quantum fluctuations of QD electrons into the attached ferromagnets and is the key factor in generating the spin resonance. Finally, the spin \mathbf{S} is subject to a spin decay, which is described by the symmetric tensor \mathcal{R}_S . The spin-decay

tensor can become significantly anisotropic in the Coulomb blockade regime due to cotunneling processes. This affects the width of the spin resonance, which we discuss in Sec. III F. Extending usual master equations in the way described above is a necessity for noncollinear spin valves, i.e., when the rotational symmetry is completely broken (see Sec. II A).

To compute all coefficients in Eq. (13), we systematically expand the kernel in the tunneling rates $\Gamma_r = 2\pi \bar{v}_r |t_r|^2$ using the real-time diagrammatic technique [52,54] and we include all leading-order Γ and next-to-leading order Γ^2 terms. This has been done analytically, starting from a general Liouville-space formulation of the real-time diagrammatic approach [54]. The resulting expressions for the rates in the above quantum master equations (13) are given in Appendix B 1. Our results extend previous works in that we account for *both* renormalization effects due to the dynamics of coherences *and* next-to-leading order Γ^2 corrections. This enables us to make reliable predictions about the spin resonance in the Coulomb blockade regime. This development was motivated by Ref. [26] where the spin resonance was found at the flank of the single-electron tunneling peak but could not be tracked into the Coulomb blockade regime because the quantum master equation used there included only leading order Γ processes. The interested reader may find details on our technical advances and how they extend previous works in Appendixes B 1 and B 2.

After solving Eq. (13) for the occupation probabilities and the average spin, one can compute the average current from lead r into the QD by

$$I_r = 2\Gamma_{r,0} p_0 - \Gamma_{r,1} p_1 - 2\mathbf{G}_{r,pS} \cdot \mathbf{S}, \quad (14)$$

where the rates are given in Appendix B 1. In Appendix B 3 we explain how to solve Eq. (13), which is actually a nontrivial task in the Coulomb blockade regime because $O(\Gamma)$ contributions can become smaller in magnitude than $O(\Gamma^2)$ contributions. With the analytical results obtained in this way, we are able to gain a physical understanding of the QD dynamics governing the spin resonance and they are, moreover, used to derive approximation formulas for the current near the resonance.

However, our analytical results are restricted to the limit $U \rightarrow \infty$. To study the case of *finite* charging energy U , we use a computer code to evaluate the kernel W numerically. The code is based on the formulas given in Ref. [52], which we extended to account for couplings between diagonal and nondiagonal density operator matrix elements to $O(\Gamma^2)$. To ensure that our perturbative approach is valid, we set for all plots $\Gamma < T$ and we further checked that the numerically computed features scale at least as $O(\Gamma^2)$ when the tunnel coupling is lowered (see also comments in Appendix B 3). Thus, the predicted spin resonance in the Coulomb blockade regime can appear in an experiment also at elevated temperatures in the sense $T > \Gamma$, for which the Kondo effect is not present.

III. STATIONARY-CONDUCTANCE RESONANCE: CHARACTERIZATION OF QUANTUM-DOT SPIN VALVES

With our model and technique established, we first turn to the discussion of the spin resonance in the stationary conductance. Here we study the generalization of Eq. (13)

to finite U and solve it numerically unless stated otherwise. We first present the most important features in the stationary conductance in Sec. III A before we scrutinize the parameter dependence of the resonance position and width in detail in the following sections. We further expound that the nontrivial parameter dependence can be used to characterize QD spin valves in an alternative way.

A. Spin resonance in stability diagram

A main result of this paper is presented in Fig. 2, which shows the stationary conductance for the setup sketched in Fig. 2(a) obtained from the extension of Eqs. (13) and (14) to finite U . We find a sharp *wiggle* in the nonlinear conductance dI/dV_b , i.e., a peak in the current plotted vs V_b , which extends through the entire Coulomb-blockade region. Notably, the resonance starts at the Coulomb diamond edge, then bends towards the particle-hole symmetry point at $(V_b = 0, \varepsilon = -U/2)$, where its magnitude vanishes, and then continues point symmetrically. We therefore focus our discussion first on the $V_g < U/2$ part of Fig. 2 and chose the labels “source” and “drain” such that the lead with the larger spin-injection rate $\Gamma_r n_r$ is the source for $V_b > 0$.

To understand the origin of the spin resonance, we note that the current through the QD is largely suppressed for antiparallel polarizations by the spin-valve effect: Electrons of spin-majority type coming from the source get stuck in the QD because they are of spin-minority type for the drain. Thus, the tunneling rate for these electrons from the QD into the drain is small. However, if the polarizations of the electrodes are merely slightly *noncollinear*, the spin resonance appears in Fig. 2. The reason for this sharp resonance is that the drain contribution to the exchange field $\mathbf{B} = B_s \hat{\mathbf{n}}_s + B_d \hat{\mathbf{n}}_d$ adds a component $B_{d,\perp} = B_d \sin \alpha$ that is perpendicular to the source polarization \mathbf{n}_s , i.e., $\mathbf{B} = (B_s + B_{d,\parallel}) \hat{\mathbf{n}}_s + B_{d,\perp} \hat{\mathbf{n}}_\perp$ with $B_{d,\parallel} = B_d \cos \alpha$ [cf. Eq. (16) below]. The seemingly innocuous component $B_{d,\perp}$ causes a precession of the spin injected along \mathbf{n}_s towards \mathbf{n}_d . Consequently, the electron can

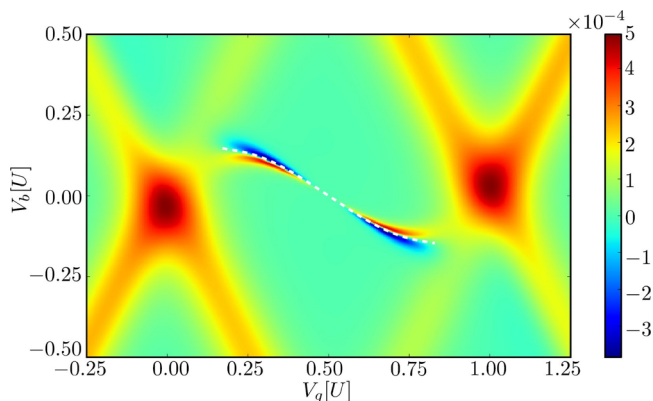


FIG. 2. (Color online) Differential conductance dI/dV_b for the setup shown in Fig. 1 for the current from the source into the QD for $\Gamma_s = 2\Gamma_d = 0.01U$, $T = 0.05U$, $W = 50U$, $n_s = n_d = 0.99$, $\alpha = 0.01\pi$. The white dashed curve follows from the resonance condition (15). Signatures in the conductance can already be found for $n_s, n_d \gtrsim 0.6$, and $\alpha < 0.4\pi$ as discussed in Sec. III B; here we use larger polarizations and smaller α for illustration purposes.

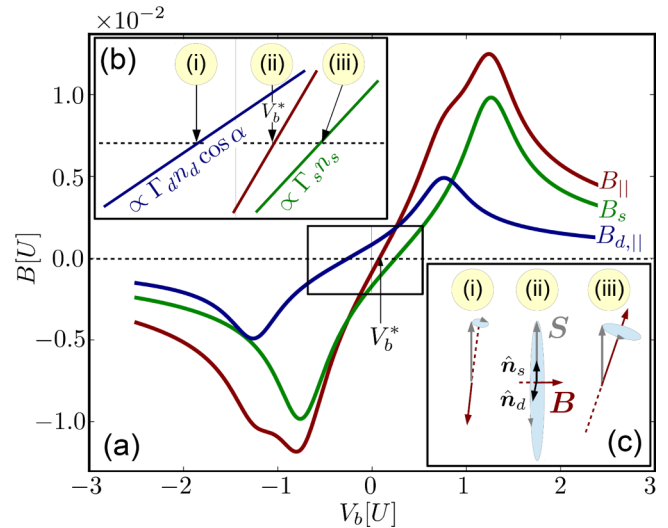


FIG. 3. (Color online) Main panel (a) and sketched zoom-in (b): Exchange field component along \mathbf{n}_s from the source electrode (B_s , green), the drain electrode ($B_{d,\parallel}$, blue), and their sum ($B_s + B_{d,\parallel}$, red) as a function of V_b for $V_g = 0.375U$, with other parameters as in Fig. 2. (c) Illustration of the spin precession (gray) for different directions of the exchange field (red), taken for different V_b as indicated in (b). The opening angle is maximal for (ii) at $V_b = V_b^*$ where Eq. (15) holds.

easily leave the QD to the drain, preventing an accumulation of spin antiparallel to the drain as expected from prior works [36,40]. We note that such a transverse component appears only because of the noncollinearity of the ferromagnets' polarizations, i.e., the complete breaking of the rotational symmetry. If the polarizations are collinear, the exchange field is aligned along the common polarization axis and therefore no spin precession is possible.

The spin-precession feature shown in Fig. 2 is unexpectedly sharp since the spin-valve effect is lifted *only* for a specific bias voltage V_b^* . The reason is that the spin rotation is effective only if the opening angle of the spin precession is large [cf. Fig. 3(c)(ii)]. Hence, the resonance appears when the total exchange field component parallel to the source polarization \mathbf{n}_s vanishes, i.e., when the following scalar condition is satisfied:

$$\mathbf{B} \cdot \hat{\mathbf{n}}_s = B_s + B_{d,\parallel} = 0. \quad (15)$$

In contrast to usual resonance conditions, it incorporates two vectors.

The resonance *position* can be predicted from the $O(\Gamma)$ approximation for the exchange field [40],

$$\mathbf{B} = \sum_r \Gamma_r \mathbf{n}_r [\phi_r(\varepsilon) - \phi_r(\varepsilon + U)], \quad (16)$$

with spin-polarization vector \mathbf{n}_r pointing in the polarization direction of the ferromagnet. Equation (16) includes the renormalization function

$$\begin{aligned} \phi_r(\varepsilon) &= \int_{-W}^{+W} \frac{d\omega}{\pi} \frac{f[(\omega - \mu_r)/T]}{\omega - \varepsilon} \\ &= \frac{1}{\pi} \left[-\text{Re} \psi \left(\frac{1}{2} + i \frac{\varepsilon - \mu_r}{2\pi T} \right) + \log \left(\frac{W}{2\pi T} \right) \right], \end{aligned} \quad (17)$$

incorporating the digamma function ψ , the Fermi function $f(x) = 1/(e^x + 1)$, and electrochemical potentials $\mu_{s,d} = \pm V_b/2$. Inserting Eq. (16) into the resonance condition (15) and solving for the resonant bias V_b^* as a function of V_g yields the white dashed curve in Fig. 2. This simple physical idea thus nicely ties in with the results of our full numerical calculations as we further work out in Sec. III C and with our analytical results based on the kinetic equations (13) for $U \rightarrow \infty$ in Sec. III F. The full theory is, however, still needed for understanding the resonance peak height and shape.

Remarkably, for a given gate voltage V_g , the condition (15) is fulfilled only for one bias polarity when the electrodes are asymmetrically coupled to the QD. This is one feature that can be used to rule out other effects in experimental data, for example, those due to inelastic cotunneling, which typically show signatures for both bias polarities. Other distinguishing features are the peak height and width as discussed in Sec. III F.

Here we first focus on the explanation of the strong current rectification, which can be attributed to the electrical tunability of the exchange field *direction*: In Fig. 3(a) we plot B_s , $B_{d,\parallel}$, and their sum $B_{\parallel} = B_s + B_{d,\parallel}$ as function of the bias V_b . For electrode r the magnitude B_r is maximal when $\mu_r = \varepsilon$ or $\mu_r = \varepsilon + U$ and vanishes midway at $\mu_r = \varepsilon + U/2$ [marked in Fig. 3(b) by (i) for $r = d$ and in (iii) for $r = s$]. In the vicinity of these points, the exchange field \mathbf{B} comes from only one electrode, pointing along \mathbf{n}_s or \mathbf{n}_d , see Figs. 3(c)(i) and 3(c)(iii), respectively. Here the spin precesses with a small opening angle and the spin transport stays blocked. However, when tuning the bias between these two cancellation points, the exchange field rotates [see Fig. 3(c)(ii)] and the sum B_{\parallel} vanishes for a specific bias voltage V_b^* and polarity. This electric tunability illustrates that renormalization-induced effective fields can intervene with the coherent evolution of two-level systems in a controlled way to produce unexpected resonances as shown in Fig. 2.

Figure 2 further clearly shows that the bias scale V_b^* does not match any obvious energy scale of the problem, attesting to its nonspectral, vectorial nature. Depending on the gate voltage, it may exceed Γ , T , and even approach a sizable fraction of U [cf. Fig. 7(a)]. As we show in Sec. III C, the effect may be exploited to characterize QD spin valves *in situ*.

Similarly, additionally attaching a superconductor to the QD, see Sec. III D, the spin-resonance position remains distinct from the energy scales set by the Andreev bound states formed on the QD [55]. The effect of the Andreev bound states is to modify the exchange field \mathbf{B} [49], which shifts the resonance position in the full calculation notably as accurately predicted by the resonance condition (15) when inserting the modified exchange field \mathbf{B} . This is explained further in Sec. III D. The above confirms that Eq. (15) truly captures the essence of the spin resonance under various situations and identifies a mechanism of a highly voltage-dependent loss of magnetoresistance for QD spin valves that is active already for small noncollinearity angles.

B. Experimental feasibility: Polarization vectors

In the above section we used large polarizations $n_s = n_d = n = 0.99$ for illustration purposes. Achieving such high values is a central goal of spintronics, yet currently presents

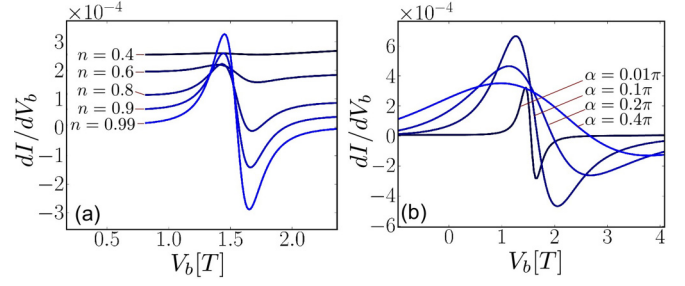


FIG. 4. (Color online) Differential conductance dI/dV_b as a function of bias voltage V_b for gate voltage $V_g = 7.5T$, varying (a) the polarization magnitude $n_s = n_d = n$ as indicated for fixed noncollinearity angle $\alpha = 0.01\pi$ and (b) varying the angle α as indicated for fixed $n_s = n_d = 0.99$. All other parameters are as in Fig. 2(a).

a challenge. However, this large value was only used to make the resonance as clear as possible in Fig. 2 but to observe our predicted feature, this is actually not needed. In Fig. 4(a) we show the nonlinear conductance dI/dV_b in the stationary state for lower values of the polarization $n = n_s = n_d$. Clearly, already for polarizations $n \gtrsim 0.6$ a discernible modification of the conductance can be seen. *In situ* polarizations as large as $n \sim 0.8$ have already been achieved with half-metallic electrodes in experiments [56].

We also note that the small noncollinearity angle $\alpha = 0.01\pi$ used in Fig. 2 shows that the assumption of perfect collinearity often made in theoretical analyses of spin-valve devices can lead to highly nongeneric results. However, the spin resonance is not limited to small noncollinearity angles: Figure 4(b) shows the conductance in the vicinity of the resonance for different noncollinearity angles α and one finds a region of negative differential conductance even for α as large as 0.4π . We conclude that it is not essential to have a noncollinearity angle very precisely close to $\alpha = 0$ and extraordinary large polarizations $n \approx 1$ to see a resonance feature in the stability diagram. Large polarizations of $n \gtrsim 0.8$ as aimed at by efforts in spintronics and angles $\alpha \lesssim 0.2\pi$ should be sufficient to observe features of the spin resonance. Moreover, Fig. 4(b) shows that the resonance position changes as a function of the angle α . This can be exploited to measure the angle α as we discuss in the next section.

C. Extracting the spin-injection asymmetry from resonance position

To investigate the parameter dependence of the resonance position systematically, we introduce the energy level detuning from the symmetry point $\varepsilon = -U/2$,

$$\delta = U + 2\varepsilon, \quad (18)$$

where the spin-resonance bias position goes through zero. As shown in Appendix C using particle-hole symmetry, it is sufficient to discuss only the case $\delta > 0$ and $V_b > 0$ since the results obtained are easily related to those for negative values. We thus limit our discussion here to the left half of the Coulomb diamond of the stability diagram in Fig. 2. We recast

the resonance condition (15) as

$$\frac{a}{q} = 1, \quad (19)$$

with the asymmetry ratio of the spin-injection rates

$$a := \frac{\Gamma_s n_s}{\Gamma_d n_d \cos(\alpha)}, \quad (20)$$

and electrically tunable ratio

$$q := \frac{\phi_d(\varepsilon) - \phi_d(\varepsilon + U)}{\phi_s(\varepsilon) - \phi_s(\varepsilon + U)}. \quad (21)$$

The above condition $a/q = 1$ has been used to generate the perfectly matching white dashed curve in Fig. 2(a) by solving it for the resonant bias V_b^* as function of V_g . Thus, we find on a numerical basis that the $O(\Gamma)$ approximation for the exchange field is sufficient to reliably predict the resonance position for the full numerical calculation up to $O(\Gamma^2)$. Deep in the Coulomb blockade regime when the distance of the electrochemical potentials from one of the level positions is large, $\min_{r=s,d}[|\varepsilon - \mu_r|, |\varepsilon + U - \mu_r|] \gg T$, the real part of the digamma function can be approximated by a logarithm, that is, $\text{Re}\Psi(1/2 + ix) \approx \ln|x|$. This leads to

$$q \approx \frac{\ln|(1 + \tilde{\delta} + \tilde{V}_b)/(1 - \tilde{\delta} - \tilde{V}_b)|}{\ln|(1 + \tilde{\delta} - \tilde{V}_b)/(1 - \tilde{\delta} + \tilde{V}_b)|}. \quad (22)$$

Thus, the factor q becomes independent of temperature and it exclusively depends on the electrical parameters such as bias through the ratio $\tilde{V}_b = V_b/U \geq 0$ and the gate voltage through the ratio $\tilde{\delta} = 1 + 2\varepsilon/U$. As a consequence, the resonance feature is just rescaled inside the Coulomb diamond when the latter is made larger by increasing the interaction energy U , cf. Fig. 5(d) below. We emphasize that the nontrivial voltage dependence of the resonance position derives from the drastic changes in the *direction* of the exchange field vector \mathbf{B} , rather than its magnitude.

To substantiate the simple condition (19) further, we next show in Fig. 5 full numerical results for the resonance when changing various parameters in the setup such that the asymmetry a remains constant. According to our prediction from Eq. (19), this leaves the resonant bias V_b^* unchanged, which is confirmed by Fig. 5. For example, when changing the tunnel couplings in Fig. 5(a) and the polarization in Fig. 5(b), the resonance width and height are affected, but the resonance bias *position* indeed stays unaltered. In Fig. 5(c) we also change the noncollinearity angle α while adapting both polarizations and tunnel couplings to keep a fixed. Finally, we increase in Fig. 5(d) the interaction energy U and find that the resonance condition (19) depends only on the ratios $\tilde{V}_b = V_b/U$ and $\tilde{\delta} = 1 + 2\varepsilon/U$ of the voltages and the interaction energy for strong Coulomb blockade conditions. By contrast, the width of the resonance changes significantly because U affects the spin-decoherence rates, see Sec. III F.

We next outline a simple procedure for determining the asymmetry a from an experimentally measured stability diagram. Here we use that the resonance condition can be drastically simplified in the vicinity of the particle-hole symmetry point. For $\tilde{\delta} \ll 1$, the condition $a/q = 1$ implies that the resonant bias also satisfies $\tilde{V}_b^* \ll 1$. Then the resonance position can be found by a linear expansion of the logarithms

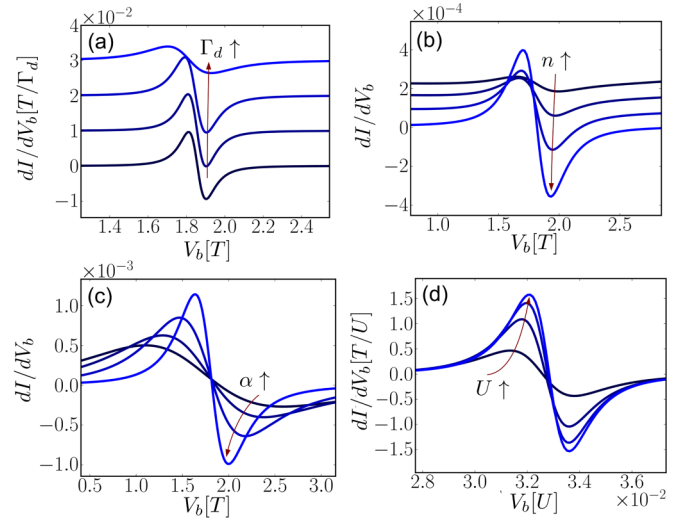


FIG. 5. (Color online) Numerically computed differential conductance dI/dV_b as a function of bias voltage V_b when modifying several parameters but keeping the spin-injection asymmetry (20) fixed. (a) The tunnel couplings are varied as $\Gamma_d = \Gamma_s/[2\cos(\alpha)] = 10^{-3}T \dots 10^{-1}T$ in four equidistant steps, keeping $n_s = n_d = 0.99$ and $\alpha = 0.01\pi$ fixed. The curves are vertically offset by 10^{-2} with respect to each other. (b) The polarization magnitudes are varied as $n_d = n_s/\cos(\alpha) = 0.6 \dots 0.99$ in four equidistant steps, keeping $\Gamma_d = \Gamma_s/2 = 0.1T$ and $\alpha = 0.01\pi$ constant. (c) The noncollinearity angle is varied as $\alpha = 0.85\pi \dots 0.97\pi$ in four equidistant steps, adjusting $\Gamma_d = \Gamma_s/[2\sqrt{\cos(\alpha)}] = 0.1T$ and $n_d = n_s/\sqrt{\cos(\alpha)} = 0.99$. The parameters in (a)–(c) are chosen such that $a = 2$, the other parameters are $U = 20T$, $V_g = 7T$, and $W = 1000T$. (d) The interaction energy is varied as $U = 40T \dots 100T$ in four equidistant steps for $n_s = n_d = 0.99$, $\Gamma_d = \Gamma_s/2 = 0.1T$, $\alpha = 0.01\pi$, $V_g = 0.45U$, and $W = 1000T$.

in Eq. (22), which results in a *linear* dependence of the resonant bias on the detuning,

$$\tilde{V}_b^* = \kappa(\alpha)\tilde{\delta}, \quad (23)$$

with slope

$$\kappa(\alpha) = \frac{a(\alpha) - 1}{a(\alpha) + 1}. \quad (24)$$

The slope (24) becomes minimal in the limit $\alpha \rightarrow 0$ (for $\alpha = 0$ the spin resonance vanishes and the slope cannot be measured). The slope increases quadratically with α as a simple expansion of Eq. (24) for small α shows and reaches $\kappa = 1$ for $\alpha = \pi/2$. Measuring the slope of the resonance position near the particle-hole symmetry point in Fig. 2 allows one to directly extract the spin-injection asymmetry $a(0) = \Gamma_s n_s / \Gamma_d n_d$ and to measure the angle α . This can be achieved in two ways: First, if one has experimental access to this slope for a single, accurately determined angle α , one can directly determine $a(0)$. Alternatively, if one has continuous control over α but the values for α are not known, one can experimentally record pairs $[\alpha_i, \kappa(\alpha_i)]$ and use Eq. (24) by inserting Eq. (20) as a fitting formula with the single parameter $a(0)$. After these two possible “calibration” procedures, one can conversely extract the angle α by measuring the slope. All this illustrates the usefulness of

the novel spin resonance as alternative and simple route for (partially) characterizing QD spin-valve setups *in situ*.

D. Impact of proximal superconductor on resonance position

To illustrate the broad applicability of our resonance concept, we study a modification of model (1) by adding a superconducting terminal at electrochemical potential $\mu_{\text{sup}} = 0$, tunnel coupled to the QD with rate Γ_{sup} , as sketched in Fig. 6(a). In the limit of infinite superconducting gap $\Delta \rightarrow \infty$, the effect of the superconductor can be incorporated by adding a pairing term

$$H_P = -\frac{1}{2}\Gamma_{\text{sup}}(d_{\uparrow}^{\dagger}d_{\downarrow}^{\dagger} + d_{\downarrow}d_{\uparrow}) \quad (25)$$

to the QD Hamiltonian (2) [57].

In the presence of a superconductor, the dependence of the leading-order exchange field on the electric parameters, contained in the ratio q [Eq. (21)], is modified: One has to replace Eq. (18) by [49]

$$\phi_r(\varepsilon) = \sum_{\gamma\gamma'=\pm} \frac{\gamma'}{2\pi} \left(1 + \frac{\gamma\delta}{2\varepsilon_A}\right) \text{Re} \Psi \left(\frac{1}{2} + i \frac{\varepsilon_{r,\gamma'\gamma}}{2\pi T}\right), \quad (26)$$

with the modified energies $\varepsilon_{r,\gamma'\gamma} = \gamma' \frac{U}{2} + \gamma \varepsilon_A - \mu_r$ due to Andreev reflection processes, incorporating the Andreev bound state energies $\varepsilon_A = \frac{1}{2}\sqrt{\delta^2 + \Gamma_{\text{sup}}^2}$ for detuning $\delta = U + 2\varepsilon$. In the limit of $\Gamma_{\text{sup}} \rightarrow 0$, Eq. (26) reduces to Eq. (18). Solving the condition $a/q = 1$ with q modified through Eq. (26) for nonzero (zero) Γ_{sup} gives the white (black) dashed curve in Fig. 6(b). Clearly the presence of the superconductor leads to a significant shift of the resonance position.

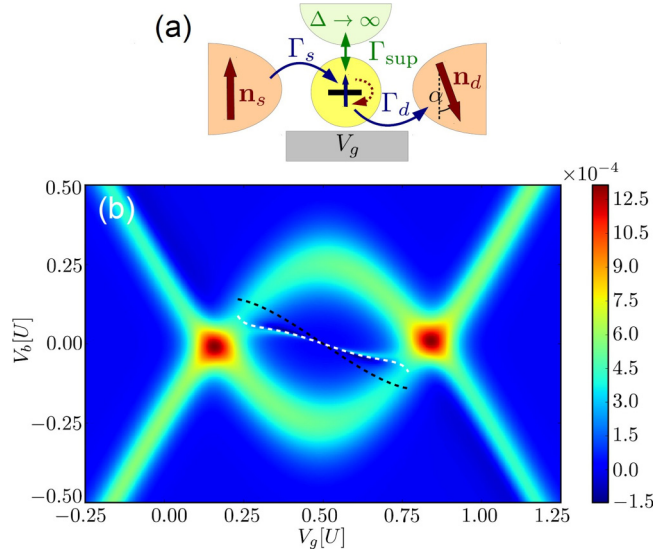


FIG. 6. (Color online) (a) Modification of the quantum-dot spin valve depicted in Fig. 1(a) including a superconducting terminal. (b) Differential conductance dI/dV_b for setup (a) for the current from the source into the QD for $\Gamma_s = 2\Gamma_d = 0.01U$, $\Gamma_{\text{sup}} = 0.75U$, $T = 0.025U$, $W = 50U$, $n_s = n_d = 0.99$, $\alpha = 0.01\pi$. The white (black) dashed curve follows from the resonance condition (15) including (excluding) the effect of the Andreev bound states. We excluded cotunneling from the calculations for (b). We comment on this in Appendix B 4.

Again approximating the real part of the digamma function deep in the Coulomb blockade regime by a logarithmic expression, we find

$$q = \frac{\sum_{\gamma=\pm} \left(1 + \frac{\gamma\delta}{2\varepsilon_A}\right) \ln \left| \frac{1+2\gamma\varepsilon_A + \tilde{V}_b}{1-2\gamma\varepsilon_A - \tilde{V}_b} \right|}{\sum_{\gamma=\pm} \left(1 + \frac{\gamma\delta}{2\varepsilon_A}\right) \ln \left| \frac{1+2\gamma\varepsilon_A - \tilde{V}_b}{1-2\gamma\varepsilon_A + \tilde{V}_b} \right|}, \quad (27)$$

with $\tilde{\varepsilon}_A = \varepsilon_A/U$. The slope $\tilde{\kappa}$ of the linear resonance condition $\tilde{V}_b^* = \tilde{\kappa}\delta$, which is valid near the particle-hole symmetry point, reads in this case

$$\begin{aligned} \tilde{\kappa}(\alpha) &= \kappa(\alpha) \ln \left| \frac{1 + \tilde{\Gamma}_{\text{sup}}}{1 - \tilde{\Gamma}_{\text{sup}}} \right| \frac{1 - \tilde{\Gamma}_{\text{sup}}^2}{2\tilde{\Gamma}_{\text{sup}}} \\ &= \kappa(\alpha)(1 - \tilde{\Gamma}_{\text{sup}}^2) + O(\tilde{\Gamma}_{\text{sup}}^3), \end{aligned} \quad (28)$$

with $\tilde{\Gamma}_{\text{sup}} = \Gamma_{\text{sup}}/U$ and κ given by Eq. (24). Hence, tuning the tunnel coupling of a proximal superconductor does not only shift the single-electron tunneling resonance positions in the stability diagram, but also suppresses the slope of the spin resonance. This can be exploited to extract the coupling to the superconductor $\tilde{\Gamma}_{\text{sup}}$ in an alternative way from the stability diagram: If the tunnel coupling Γ_{sup} can be effectively suppressed, which leads from Fig. 6(b) to Fig. 2, one can obtain $\tilde{\Gamma}_{\text{sup}}$ from Eq. (28) by inserting the experimentally measured values for $\kappa(\alpha)$ and $\tilde{\kappa}(\alpha)$. This may be advantageous since the broadening of the spin resonance can be much smaller than that of the single-electron tunneling resonances, as demonstrated by Fig. 6(b). If one has additional control over the angle α , the broadening of the spin resonance due to cotunneling processes, which are not included in Fig. 6(b), can be compensated by reducing α , see Sec. III F.

We finally comment on our assumption of an infinite superconducting gap Δ . In experiments, the gap Δ can be ~ 1 meV and therefore on the order of typical charging energies [58]. Hybrid superconductor-ferromagnetic structures have also been realized with somewhat smaller gaps of $\sim 100 \mu\text{eV}$ [59]. However, as long as the bias V_b is smaller than Δ and the Andreev bound state energies, real tunneling processes due to the superconductor are strongly suppressed and renormalization effects due to quantum fluctuations dominate. This expectation is underpinned by a recent theoretical study [60] which considers corrections to the infinite-gap approximation by expanding in $1/\Delta$. It turns out that the main effect of the finite gap is to shift the Andreev bound state energies rather than leading to modifications of the current. Therefore, we expect that the form of our resonance condition (15) should be valid for finite Δ when tuning close to the particle-hole symmetry point where the resonance appears for small bias.

Our study thus illustrates a new, fruitful, and experimentally relevant interplay of superconductivity and spintronics. Exploring the situation of a finite superconducting gap Δ when $V_b \sim \Delta$ is an interesting open question that presents additional technical challenges beyond the scope of this paper. For the rest of this paper we return to the case when no superconducting leads are present, i.e., $\Gamma_{\text{sup}} = 0$.

E. “Half-sided Coulomb diamond” and zero-bias peak

As just illustrated by the superconducting hybrid setup, the spin resonance position sensitively reacts to modifications

of the exchange field through the ratio q regulating the dependence on voltages. However, the resonance position can also be changed by the other factor in Eq. (19), the spin-injection asymmetry a . We illustrate this for the two extreme cases leading to transport stability diagrams which would be puzzling if one were to experimentally obtain them without having further microscopic information: For very large asymmetries, $a \gg 1$, the resonance becomes parallel to Coulomb edges, forming a “half-sided Coulomb diamond,” whereas for negligible asymmetry, $a = 1$, the resonance appears as a zero-bias conductance peak. Even though the Kondo resonance and the zero-bias anomaly of Refs. [24,28] also appear at zero bias, our spin resonance is clearly distinguished from these features as we explain below.

We first note that the resonance position can appear in the entire voltage range by changing κ through the tunneling rates, polarizations, and the angle α , limited only by the condition

$$0 \leq \tilde{V}_b^* \leq \tilde{\delta} \quad (\tilde{\delta} > 0) \quad (29)$$

if the electrode with the larger spin injection rate becomes the source for $V_b > 0$ and if $\alpha < \pi/2$ (which is needed for a sharp feature). The restriction (29) is readily proved from Eq. (19): Since the asymmetry parameter $a = \Gamma_s n_s / [\Gamma_d n_d \cos(\alpha)] \geq 1$, it follows that $q \geq 1$. The parameter q has a magnitude larger than 1 if the numerator in Eq. (19) is larger than that of the denominator, which implies $\tilde{V}_b^* \geq 0$. For q to be positive, one additionally has to demand $\tilde{V}_b^* \leq \tilde{\delta}$ since $\tilde{\delta} \geq 0$. The analogous constraint in the other half of the Coulomb-blockade region,

$$\tilde{\delta} \leq \tilde{V}_b^* \leq 0 \quad (\tilde{\delta} < 0), \quad (30)$$

follows by similar arguments (see Appendix C). The above inequalities turn into an equality for the two extreme cases illustrated in Fig. 7.

First, we show the resonance in Fig. 7(a) for strong asymmetry $a \gg 1$. Here the resonance position is at $\tilde{V}_b^* = \tilde{\delta}$, i.e., parallel to the Coulomb diamond edges. Strikingly, the resonance is much sharper than the temperature-broadened single-electron tunneling resonances because the width is not simply limited by temperature T and tunnel coupling Γ (see Sec. III F). If one were to measure such a signature and would have no further microscopic information one would thus wonder why this feature is not thermally broadened, whereas the others can be demonstrated to change with temperature.

Second, in Fig. 7(b) we show the resonance for perfect symmetry $a = 1$, in which case it appears at $\tilde{V}_b^* = 0$ and only for an odd number of electrons on the QD. This signature could in fact be mistaken for features due to the Kondo effect for electrodes with negligible polarization or the zero-bias anomaly discussed in Refs. [24,28], which are otherwise very dissimilar. One should note that the Kondo effect requires strong tunnel couplings ($\Gamma/T \gg 1$), whereas the spin resonance also appears in the intermediate coupling regime (still $\Gamma/T < 1$). Moreover, the spin resonance disappears at the particle-hole symmetry point, while the Kondo effect can remain at this point. It can even appear *only* at this point for strong, parallel spin polarizations of the electrodes [32,34,37,61] since the exchange field $\mathbf{B} = \mathbf{0}$ there. (For the case of strong magnetizations of the electrodes this is no longer true [35].) For strong, antiparallel polarizations—the configuration close to where the spin resonance occurs—it

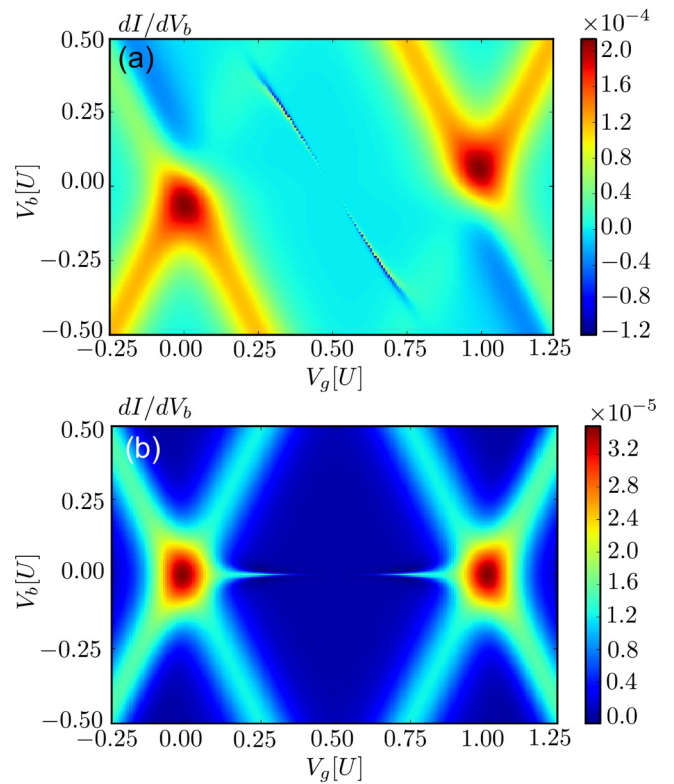


FIG. 7. (Color online) Differential conductance dI/dV_b as a function of gate voltage V_g and bias voltage V_b . In (a), the spin-injection ratio is $a = 10$ with $\Gamma_s = 0.1/\sqrt{\cos(\alpha)}$ and $\Gamma_d = 0.01/\sqrt{\cos(\alpha)}$ and in (b) the spin-injection ratio is $a = 1$ with $\Gamma_s = \Gamma_d = 0.01\sqrt{\cos(\alpha)}T$. All other parameters are as in Fig. 2.

depends on the asymmetries of the spin-injection rates whether the Kondo effect emerges or not.

Furthermore, for symmetric spin-injection rates, one should also not mistake the spin resonance for the zero-bias anomaly studied in Refs. [24,28], caused by the interplay of the voltage dependence of the cotunneling spin-flip rates with the spin-valve effect. Both effects can in fact appear together and, as we demonstrate in Fig. 8, the spin resonance may be even much larger and sharper than the zero-bias anomaly. However, it depends on the choice of the parameters which of the two is more pronounced: For example, while the width of the zero-bias anomaly is set by temperature, the width of the spin resonance is independent of T and determined instead by the angle α and a combination of the spin-decay rates and the exchange field, which depends strongly on the applied gate voltage (see Sec. III F). Moreover, in contrast to the spin resonance, the zero-bias anomaly persists at the particle-hole symmetry point and for strictly antiparallel lead polarizations.

The above illustrates that our spin resonance is really an independent conductance feature, distinct from other features and can moreover be identified unambiguously in an experiment.

F. Extracting the anisotropy of the spin-decay tensor from the resonance shape

Besides the resonance position we have focused on so far, the resonance shape provides additional valuable information

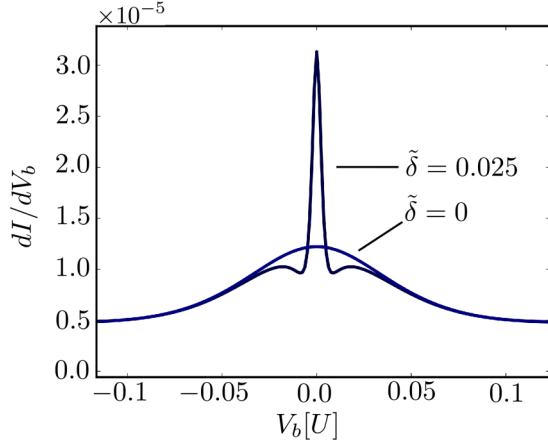


FIG. 8. (Color online) Differential conductance dI/dV_b as a function of bias voltage V_b for $\Gamma_s = \Gamma_d = 0.5T$, $n_s = n_d = 0.99$, $\alpha = 0.01\pi$, $U = 40T$, and $W = 1000T$. For the gate voltage that restores the particle-hole symmetry, $\tilde{\delta} = 0$, the spin resonance is absent and the broad zero-bias anomaly of Refs. [24,28] is visible. For $\tilde{\delta} = 0.025$, when the particle-hole symmetry is absent, the conductance profile for small bias is by contrast completely dominated by the spin resonance. We chose here rather larger tunnel couplings to compare with the above-cited references. We note that the conductance is shown there for strictly antiparallel polarizations, $\alpha = 0$, which has negligible impact on the zero-bias anomaly as compared to the case $\alpha = 0.01\pi$ considered here. Note that the zero-bias anomaly does not appear in Fig. 7 because the tunnel couplings are smaller there, yet our spin resonance persists for these parameter values.

about the QD spin valve: In particular, one can extract information about the anisotropy of the spin-decay rates, that is, the spin-relaxation rate $\Gamma_{\parallel} = \hat{\mathbf{n}}_s \cdot \mathcal{R}_S \cdot \hat{\mathbf{n}}_s$ and the spin-dephasing rate $\Gamma_{\perp} = \hat{\mathbf{n}}_{\perp} \cdot \mathcal{R}_S \cdot \hat{\mathbf{n}}_{\perp}$, where $\hat{\mathbf{n}}_{\perp}$ is a unit vector perpendicular to $\hat{\mathbf{n}}_s$. In contrast to the position, the shape is significantly influenced by cotunneling corrections and crucially relies on the technical developments we report.

To illustrate this, we now restrict our attention to voltages near the resonance (such that $B_{\parallel}/B_{\perp} \lesssim 1$) in the limit of strong Coulomb blockade ($V_b/2\varepsilon \ll 1$ and $U \rightarrow \infty$), small noncollinearity angles ($\alpha \ll 1$), symmetric polarization magnitudes $n_s = n_d = n$, and small spin injection asymmetry ($\kappa \ll 1$). In this case, the stationary current (14), $I = I_s = -I_d$, flowing through the QD can be approximated by

$$I^{\text{appr}} = I_0[1 - A(1 - M)], \quad (31)$$

with

$$I_0 = \frac{\sum_{r,\tau} r(-1)^{\tau} \Gamma_{r,\tau} \Gamma_{\bar{r},\bar{\tau}}}{2\Gamma_0 + \Gamma_1}, \quad (32)$$

$$A = 2 \frac{\sum_{r,\tau} r(-1)^{\tau} (\mathbf{G}_{r,pS} \cdot \hat{\mathbf{n}}_s) (\mathbf{G}_{Sp}^{\tau} \cdot \hat{\mathbf{n}}_s) \Gamma_{\bar{r},\bar{\tau}}}{\sum_{r,\tau} (-1)^{\tau} \Gamma_{\parallel} \Gamma_{r,\tau} \Gamma_{\bar{r},\bar{\tau}}}, \quad (33)$$

$$M = \frac{M_0}{1 + [(a/q - 1)/H]^2}, \quad (34)$$

where all rates are defined in Appendix B 1. Here τ takes the values 0 and 1, $\bar{\tau} := 1 - \tau$, and the factor r in the above sums

takes the value $r = +$ ($r = -$) for $r = s$ ($r = d$) and $\bar{r} = -r$. Finally, we introduced the abbreviations

$$M_0 = \frac{1}{1 + (\Gamma_{\parallel} \Gamma_{\perp})/B_{\perp}^2}, \quad (35)$$

$$H = \alpha \sqrt{\frac{\Gamma_{\perp}}{\Gamma_{\parallel} M_0}}. \quad (36)$$

Equation (31) can be interpreted as follows: The value I_0 is the current obtained when ignoring the spin accumulation, that is, forcing “by hand” $\mathbf{S} = 0$ in the kinetic equations (13). Note that I_0 does not coincide with the current for zero polarization since the charge-relaxation rates (B2) also depend on the polarizations. The actual nonzero spin accumulation $\mathbf{S} \neq 0$ on the QD acts back on the charge dynamics, thus suppressing the current to a fraction $1 - A < 1$ of the current I_0 . However, for any nonzero α the exchange-field induced spin precession can in turn suppress this spin-valve effect. This is captured by the factor $1 - M$, where M is a Lorentzian function in the parameter $a/q - 1$ with intensity M_0 and width H . The current becomes maximal at $a/q = 1$, which is the resonance condition (19).

The peak value of the current resonance depends on two competing influences of the cotunneling contributions to the current: On the one hand, they increase the maximally achievable current I_0 by providing additional tunneling processes, but on the other hand they enhance the spin decay, which limits the effectiveness of the spin precession by suppressing M_0 and thereby M . The decisive parameter that controls the current peak value is the ratio

$$b := |B_{\perp}|/\sqrt{\Gamma_{\perp} \Gamma_{\parallel}} \quad (37)$$

of the perpendicular exchange field component and the spin-decay rates. Notably, the spin resonance appears both for (i) the strongly underdamped case $b \gg 1$ and for (ii) the critically damped case $b \sim 1$, while it disappears for (iii) the strongly overdamped case when $b \ll 1$, where $M_0 \rightarrow 0$ and therefore M has negligible impact on the current. The “optimal” value for a maximal current enhancement is given for $b \approx 1$. However, even for $b < 1$ but not yet $b \ll 1$, the spin precession can still significantly enhance the current to produce a sharp feature in the conductance as in Fig. 2. Therefore, the occurrence of the spin resonance in the *stationary* conductance is *not* yet evidence of an underdamped spin precession. By contrast, the pulsing scheme discussed below in Sec. IV A is able to unambiguously demonstrate underdamped spin precession.

Before discussing the time-dependent results, we first compare the stationary features in cases (i) and (ii) and moreover explain how they can be exploited to extract the spin-decay properties from electron transport measurements. A salient finding of this scheme is that the electrical tunability of the exchange field allows for an *all-electric* probing of the anisotropic spin-decay tensor \mathcal{R}_S *in situ*. This scheme resembles that of Ref. [46] where the interplay of the exchange field with an external perpendicular magnetic field was used to extract the spin-dephasing rate. Here one utilizes the built-in exchange field instead.

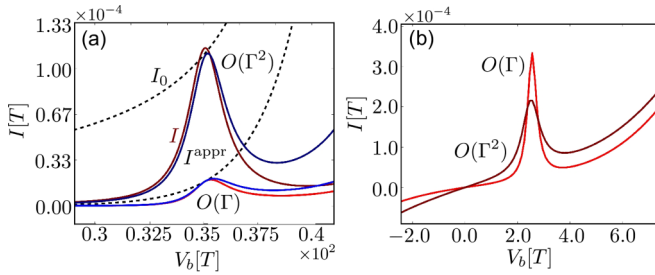


FIG. 9. (Color online) Stationary current as a function of bias voltage V_b up to $O(\Gamma)$ and $O(\Gamma^2)$ as indicated. (a) Strongly underdamped case ($b \gg 1$) in the large- U limit. The current is computed first numerically from the extension of Eq. (13) to the finite- U case for $U = 1000 T/3$ (red, denoted by I) and approximated by formula (31) in the limit of $U \rightarrow \infty$ (blue, denoted by I^{appr}). We also show the current (32) for zero spin accumulation (dashed black line, denoted by I_0). The other parameters are $V_g = 75 T/3$, $\Gamma_s = 2\Gamma_d = 0.2 T/3$, $n_s = n_d = 0.99$, $\alpha = 0.01\pi$, and $W = 1000 T/3$. This choice of parameters implies $b \gtrsim 5$ [given by Eq. (37)] for both $O(\Gamma)$ and $O(\Gamma^2)$ at the resonance. The approximated current and the numerically computed current match well but not perfectly. The main reason for the deviation is that the resonance does not appear here under strong Coulomb blockade conditions, as required for Eq. (31) to be strictly valid. These conditions are met in Fig. 10(b) below, where approximation and numerical solution match perfectly. However, if we go deeper into the Coulomb blockade regime here, the resonance disappears in $O(\Gamma)$, cf. Ref. [26]. Therefore, to make a comparison between the $O(\Gamma)$ and $O(\Gamma^2)$ current, we considered the resonance closer to the single-electron tunneling regime. (b) Critically damped case ($b \approx 1$) in the finite- U case: Stationary current up to $O(\Gamma)$ and $O(\Gamma^2)$ as a function of bias voltage V_b numerically calculated from Eq. (13) for $V_g = 5T$ with all other parameters as in Fig. 2, implying $b \approx 0.5$ for $O(\Gamma)$, $b \approx 0.2$ for $O(\Gamma^2)$. Note that our approximation formula (31) cannot be applied for the finite- U case employed here.

(i) *Underdamped regime* ($b \gg 1$). In this regime the current is restored to the full value I_0 at resonance ($a/q = 1$) since $M_0 \approx 1$. This is illustrated in Fig. 9(a), in which we plot the current numerically obtained from Eq. (13) extended to finite U and the approximation formula (31). Both are close to the value of I_0 (black dashed line) at the resonance. Both agree well, but not perfectly, as we explain further in the caption of Fig. 9. The resonance width

$$H \approx \alpha \sqrt{\frac{\Gamma_{\perp}}{\Gamma_{\parallel}}} \quad (38)$$

directly yields the anisotropy of the spin-decay tensor $\Gamma_{\perp}/\Gamma_{\parallel}$ when the angle α is known. To extract $\Gamma_{\perp}/\Gamma_{\parallel}$ from experimental data, one first determines the spin-injection asymmetry a from the resonance position, as described in Sec. III C. One then fits Eq. (31) to gate or bias traces of the current peak, expressing $a/q - 1$ with the help of Eq. (22) as a function of bias and gate voltage. In the resulting expression, the functions I_0 , H , and A appear. For fitting to experimental data, we suggest to treat these slowly varying functions as constant fitting parameters near the resonance.

(ii) *Critical damping* ($b \approx 1$). When the spin-decay rate is comparable to the spin-precession rate, the current peak value is not completely restored to I_0 as M_0 reaches only

a fraction of 1. Here the spin decay limits the maximally achievable rotation angle for the QD spin before it decays or tunnels out. This is visible in Fig. 9(b), where the peak current may become *smaller* in $O(\Gamma^2)$ as compared to that in $O(\Gamma)$, where the spin decay is much slower. Furthermore, cotunneling corrections affect the width H more strongly than in the strongly underdamped regime: Here the width is not exclusively determined by the ratio $\Gamma_{\perp}/\Gamma_{\parallel}$ but also incorporates b , which differs depending on whether cotunneling corrections are included or not. This illustrates that—in contrast to the resonance position—for the accurate prediction of the resonance shape the next-to-leading order corrections are indispensable. The pronounced sensitivity of the resonance to cotunneling processes in the critically damped limit $b \approx 1$ is also interesting for the characterization of the QD spin valve: Once B_{\perp} is determined, e.g., from the pulsing scheme (see Sec. IV), we may again use Eq. (31) as fitting formula, taking M_0 now as an additional fitting parameter. One may then extract the spin relaxation rate Γ_{\parallel} and the dephasing rate Γ_{\perp} *individually* by combining the results for H and M_0 .

IV. GATE-PULSING SCHEME: ALL-ELECTRIC SINGLE-SPIN OPERATIONS

In principle, the transport-induced spin decoherence time $\sim U/\Gamma^2$ can be made comparable or longer than experimentally measured spin-dephasing times due to other mechanisms (see Sec. IV C) by reducing the tunneling rates. Hence, multiple revolutions of an individual QD spin are feasible. Probing this underdamped spin precession requires time-resolved measurements. At first sight, it may seem challenging to utilize our transport setup for spin detection: Many spin-to-charge conversion readout schemes rely on a large energy splitting $B \gg T$ between the two spin states allowing the QD electron to leave into an attached electrode only if it has one type of spin. However, as there is no discernible spin splitting in our case, such an energy-selective readout scheme [62] is not applicable here. We therefore suggest to employ a tunneling-rate selective readout [62], which is naturally provided by the strongly spin-polarized ferromagnets in our setup. As we predict in Sec. IV A, this only requires the adaptation of an experimentally well-developed pulsing scheme [63]. Using this scheme, underdamped oscillations in the *time-averaged current* can be probed as a function of the pulsing duration. To optimize the contrast in the average current oscillations, the pulsing durations have to be chosen appropriately as we explain in Sec. IV B.

In contrast to other transport transport features in the Coulomb blockade regime, such as the Kondo effect or the zero-bias anomaly discussed in Refs. [24,28], the spin resonance does not destroy the coherence of the QD spin. This is an advantage as it allows all-electric spin control to be accomplished even without the need of an external magnetic field or spin-orbit interaction. Only the basic tool of spintronics is required: large polarizations of the ferromagnets.

A. Probing underdamped spin precession from average current

The procedure of the simple pulsing scheme is sketched in Fig. 10(a): At fixed bias voltage V_b , one repeatedly applies a

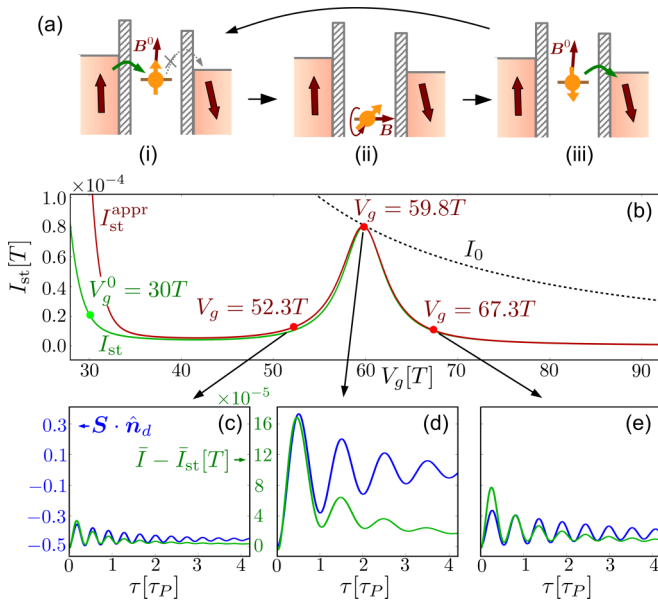


FIG. 10. (Color online) (a) Schematics of the pulsing scheme. (b) Stationary current as function of V_g , obtained by solving Eq. (13) exactly (I_{st} , green), by neglecting the spin accumulation, i.e., forcing $\mathbf{S} = 0$ (I_0 , dashed black), and by taking the approximation (31) near resonance (I_{st}^{appr} , red), see Sec. III F. (c)–(e) Average current $\bar{I} = \int_0^t (dt'/t) I_s(t')$ ($t \gg \tau, \tau^0$) (green curves) as a function of τ for three different V_g as indicated and for fixed $\tau^0 = 2 \times 10^3/T = 0.46\tau_p$, and $V_g^0 = 30T$. The times τ^0 and τ are given in units of the precession period at resonance, $\tau_p \approx 4.7 \times 10^3/T$. The current is offset by \bar{I}_{st} , the current that would flow if the QD were in the stationary state at each instant of time. Also plotted is the spin component along the drain polarization $\mathbf{S} \cdot \hat{\mathbf{n}}_d$ (blue curves) computed from Eq. (13) for initial condition $\mathbf{S} = \hat{\mathbf{n}}_s/2$ and $p_1 = 1 - p_0 = 1$. Throughout we used $n_s = n_d = 0.99$ (see caption of Fig. 2), $\alpha = 0.005\pi$, $V_b = 50T$, $W = 500T$, $\Gamma_s = 0.15T$, $\Gamma_d = 0.1T$. The plots are obtained by numerically solving the analytically derived kinetic equations (13) in the limit $U \rightarrow \infty$ using the scheme discussed in Appendix B 3. To make use of analytical results, we need a tiny angle α here. For finite U , this restriction is unnecessary.

rectangular voltage pulse to the gate electrode, switching from V_g^0 to V_g for a time duration τ , and then back to V_g^0 for a time duration τ^0 . Figure 10(b) shows the stationary current as function of V_g , exhibiting the spin resonance. We suggest to probe the time-averaged current over many pulses,

$$\bar{I} = \int_0^t \frac{dt'}{t} I_s(t') \quad (t \gg \tau, \tau^0), \quad (39)$$

varying the time duration τ . Figures 10(c)–10(e) illustrate that the time-averaged current oscillates as a function of τ with a period given by $2\pi/|\mathbf{B}|$, which coincides with the period of the plotted spin oscillations. Thus, one can extract the magnitude of the exchange field $|\mathbf{B}|$ at (V_b, V_g) . The oscillations can be physically understood as follows: By switching from the spin-valve blocked reference voltage V_g^0 [with field \mathbf{B}^0 nearly collinear with \mathbf{n}_s , cf. panel (i) in Fig. 10(a)] to a voltage V_g where the exchange field \mathbf{B} precesses the injected spin, the electron is more probable to escape upon return to V_g^0 provided

the duration τ matches a half-integer multiple of the precession time $\tau_p = 2\pi/|\mathbf{B}|$.

We compute the average current shown in Figs. 10(c)–10(e) as follows: Taking the stationary state at V_g^0 as initial state $\rho(0)$, we obtain the time-dependent solution for $\rho(t)$ by solving the kinetic equations (13). This yields the time-dependent particle current $I_s(t)$ from Eq. (14). For both the current and the kinetic equations the rates are time-dependently switched by changing the gate voltage $V_g^0 \leftrightarrow V_g$ in the respective expressions according to the pulsing scheme. To ensure that Eq. (39) really gives the current measured in a circuit, we checked that $\dot{p}_1(t) \ll |I_s(t)|, |I_d(t)|$, i.e., the magnitudes of the currents flowing out of the source, $|I_s(t)|$, and into the drain, $|I_d(t)|$, are nearly the same. Under this condition displacement currents can be neglected, as explained, for example, in Ref. [64]. We comment in Appendix B 5 on the importance of non-Markovian corrections that we neglect here.

The key feature of the current oscillations shown in Figs. 10(c)–10(e) is that the visibility strongly depends on the voltage V_g controlling the opening angle of the precession. The visibility becomes maximal at the resonance in Fig. 10(d). To prove our claim that the current oscillations are correlated with a spin precession, we compare in Figs. 10(c)–10(e) the time-averaged current with time-dependent spin-projection curves, which are obtained as follows: We take the initial state $\rho(0)$ to be the maximally polarized state with spin $\mathbf{S} = \hat{\mathbf{n}}_s/2$ and corresponding occupation probabilities $p_1 = 1$ and $p_0 = 0$, i.e., we do not start from the stationary state at gate voltage V_g . We then solve the kinetic equations (13) time dependently, keeping the gate voltage fixed at V_g . The resulting spin vector $\mathbf{S}(t)$ is then projected on the drain polarization direction $\hat{\mathbf{n}}_d$, which yields the different spin projection curves $\mathbf{S}(t) \cdot \hat{\mathbf{n}}_d$ in Figs. 10(c)–10(e) with $\tau = t$. This comparison shows that the current actually oscillates with the same frequency with which a spin would precess in a QD held at gate voltage V_g .

Finally, by going slightly off-resonance the precession axis can be fully tuned within the plane of polarizations while maintaining full control over the precession angle through τ . This allows all single-spin operations required for quantum algorithms to be implemented.

B. Optimizing the pulsing scheme

To set up an experiment that probes the underdamped spin precession, we provide here some additional information under which conditions the contrast of the signal obtained by the pulsing scheme is maximized. For this purpose, we discuss the ratio \bar{I}/\bar{I}_{st} of the time-averaged current (39) from the pulsing scheme \bar{I} to the stationary current \bar{I}_{st} . The latter is obtained by replacing the time-dependent current $I_s(t) = I_{st}[V_g(t)]$ in Eq. (39) by the stationary current, switching only the gate voltage V_g as a parameter time dependently.

First, underdamped precession cycles of a single spin are feasible only if the spin-decay rate is much smaller than the spin-precession rate at the resonance (see Sec. III F), that is, if

$$b = |B_\perp|/\sqrt{\Gamma_\perp \Gamma_\parallel} \gg 1. \quad (40)$$

This condition is different from the condition that maximizes the stationary current, cf. Sec. III F. There we found a ratio $b \sim 1$ to be optimal because then roughly one revolution

takes place within the average electron dwell time on the QD. If the tunneling rate allows for multiple precession cycles, the stationary resonant current is suppressed again because tunneling happens infrequently, even if its spin has optimal overlap with the drain polarization. This current suppression near the resonance does not appear for the gate-pulsing scheme since one returns to a gate voltage V_g^0 closer to the single-electron tunneling resonance where the tunneling rate is larger and the electron can leave the QD quickly after it has been precessed at gate voltage V_g . Thus, the larger the ratio b , the clearer the current oscillations are and the longer they persist.

The second important set of parameters that has to be optimized are the dwell times τ^0 and τ at voltage V_g^0 and V_g . A first requirement is that

$$\tau^0 \lesssim \tau \quad (41)$$

because if $\tau^0 \gg \tau$ the system is most of the time not at resonance and the average current is determined by the dynamics at gate voltage V_g^0 . Condition (41) is fulfilled for most values of τ shown in Fig. 10. However, there is another condition that is equally important: We find on a numerical basis that τ^0 is chosen optimally as

$$\tau^0 \approx 0.1\tau_T^0 \approx 0.1/I_{st}^0, \quad (42)$$

with the electron dwell time τ_T^0 at gate voltage V_g^0 , which can be estimated by the inverse of the stationary particle current I_{st}^0 at voltage V_g^0 . If $\tau^0 \gtrsim \tau_T^0$, the average current is mostly determined by the large stationary current I_{st}^0 , i.e., the precession-induced initial modification of the current at V_g^0 is rather insignificant. This is illustrated in Fig. 11(a), in which we plot the ratio of the average current \bar{I} obtained from the pulsing scheme and the average current \bar{I}_{st} that is obtained if the QD was in the stationary state all the time (but switching between the different levels at the two gate voltages): Clearly, for small (but not very small) times τ^0 , the

current is drastically enhanced over the stationary current due to the gate pulsing, while the ratio decreases if τ^0 approaches τ_T^0 . In Fig. 10 we use a value $\tau^0/\tau_T^0 \sim 1$, which already yields a sizable enhancement.

However, if $\tau^0 \ll \tau_T^0$, the ratio \bar{I}/I_{st} becomes drastically suppressed as Fig. 11(a) also shows. In this case, the QD electron does not have enough time to tunnel out of the QD when the gate voltage is switched to V_g^0 . The average current is then mostly determined by the time-averaged current at resonance. This is illustrated in Fig. 11(b), which shows the time-dependent current $I_s(t)$ (blue) besides its average current \bar{I} (green), which loses contrast after roughly two cycles.

We conclude that for setting up and optimizing the pulsing scheme in an experiment, the initial characterization of the spin valve is of the utmost importance. Once the time scales are known our above discussion should be a guide to choose the pulsing times properly.

C. Experimental feasibility: Spin decoherence

Finally, we provide rough estimates for the spin-decay times and spin-precession periods for experimentally achievable parameters, demonstrating the feasibility of underdamped spin-precession cycles in the Coulomb blockade regime. Typical spin-dephasing times of $\sim 10 - 30$ ns have been measured in GaAs QDs [4,7,65] and are also compatible with measurements involving carbon nanotubes (CNTs) [56]. In our case, the cotunneling current through the QD leads to additional dephasing with time constant $\sim U/\Gamma^2 \sim 10/\mu\text{eV} \sim 30$ ns for typical values of $\Gamma \sim 0.01$ meV and $U \sim 5$ meV feasible both for semiconductor QDs and CNT QDs. The energy scale related to the exchange field may be estimated as $\mu_B B > \mu_B B_{d,\perp} \approx \mu_B |\log(1/2)|\Gamma_d n_d \sin \alpha/\pi \sim 0.7 \mu\text{eV}$ for $n_d \sim 0.5$ and $\alpha \sim 0.2\pi$. This translates into a maximal precession period of $T \sim 2\pi/0.7 \mu\text{eV} \sim 6$ ns at the resonance and even smaller periods away from it. Thus, indeed the spin-precession period can be made smaller than the spin-decay time.

One may wonder whether the spin resonance could also be observed in the strong-coupling regime $\Gamma \gg T$. This regime has been under intense experimental investigation (using collinear polarizations so far) since the exchange field can be probed there by the strong spin splitting it induces, affecting the Kondo resonance [33–35]. Increasing the tunnel coupling Γ , however, enhances the spin-decoherence rate more strongly than the spin-precession rate. Moreover, spin-flip processes driving the Kondo effect for small bias voltage also destroy the QD spin coherence. Thus, the spin precession may not be underdamped any more in the strong coupling regime. In addition, the smaller spin-precession periods, which are approximately ~ 100 ps as extracted from exchange-field magnitudes in Ref. [34], makes it more challenging to apply the pulsing scheme described above. By contrast, spin-resonance features are more likely to be seen in the stationary current, which requires the spin-precession rate only to be comparable to the spin-decoherence rate. The reader should note that the width of the spin resonance can be much smaller than the spin-decoherence rate as our analysis in Sec. III F shows. Thus, it is worth investigating the spin resonance in the strong-coupling regime further. We

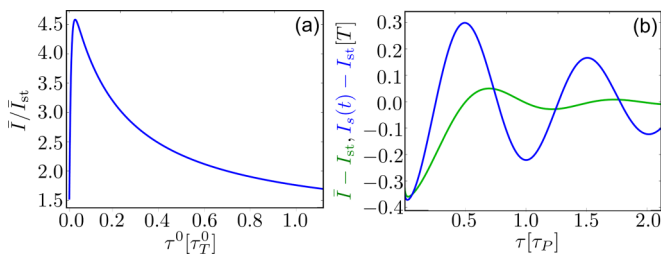


FIG. 11. (Color online) (a) Ratio \bar{I}/I_{st} as a function of the duration τ^0 in units of the electron dwell time $\tau_T^0 = 1/I_{st}^0 \approx 4.7 \times 10^4/T$. Here \bar{I} is the average current (39) for the pulsing scheme and \bar{I}_{st} is the stationary current obtained if the QD was in the stationary state all the time. The gate voltage $V_g = V_g^* = 59.8T$ is tuned to the resonance and $\tau = 2500/T \approx 0.53\tau_P$ so that a nearly maximal enhancement of the current occurs after the precession. (b) Average current \bar{I} and time-dependent current $I_s(t)$ as function of the pulse time τ with $\tau_P \approx 4.7 \times 10^3/T$ and $\tau^0 = 10/T = 2.1 \times 10^{-3}\tau_P \ll \tau$. We subtract the stationary current I_{st} flowing at gate voltage $V_g = V_g^*$. The results shown in (a) and (b) are computed for a single pulse, $N = 1$ [$t = \tau^0 + \tau$ in Eq. (39)], and all other parameters are the same as in Fig. 10.

finally note that recently, signatures of the spin resonance have also been found by one of the authors in waiting-time distributions [66].

V. SUMMARY AND OUTLOOK

We have identified a spin resonance that, unlike usual resonances, does not appear when scalar energies of the local quantum system and reservoir match. Instead, the condition (15) based on vectors $\mathbf{B} \cdot \hat{\mathbf{n}}_s = 0$ needs to be satisfied. The resonance emerges in the simplest QD spin-valve setup one can think of: an interacting spin-degenerate single level which is tunnel coupled to two ferromagnets for *almost* (but not exactly) antiparallel polarizations \mathbf{n}_s and \mathbf{n}_d . For this magnetic configuration, the direction of the exchange field \mathbf{B} strongly depends on the applied voltages, which generates a sharp feature all across the Coulomb diamond of the transport stability diagram.

The resonance is clearly distinguished from other features in the stability diagram: First, it emerges only for nonzero noncollinearity angle α and responds sensitively to changes in α . Second, it depends strongly on the asymmetries of the spin-injection rates. For small asymmetries, it exhibits a strong current rectification effect while for symmetric spin-injection rates it lies at zero bias. Third, when these parameters cannot be controlled in an experiment, one can use the peculiar voltage-dependent line shape of the spin resonance to tell it apart from other features. For example, the spin resonance vanishes at the particle-hole symmetry point. Furthermore, its width is not given by a simple combination of the tunnel couplings, temperature, or any other natural energy scale. Instead, it depends on the ratio of the gate-voltage dependent exchange field and the spin-decay rates. The latter features contrast particularly with those from the Kondo effect or the zero-bias anomaly predicted earlier in Refs. [24,28].

While the resonance position is entirely dictated by the exchange field *direction*, the shape of the resonance (peak value, width) is strongly influenced by the QD spin decay. We have identified the ratio $b = |B_\perp|/\sqrt{\Gamma_\perp\Gamma_\parallel}$ to be the relevant parameter that determines the resonance shape. This ratio involves the perpendicular exchange field component $B_\perp = \mathbf{B} \cdot \hat{\mathbf{n}}_\perp$, the spin-relaxation rate $\Gamma_\parallel = \hat{\mathbf{n}}_s \cdot \mathcal{R}_S \cdot \hat{\mathbf{n}}_s$, and the spin-dephasing rate $\Gamma_\perp = \hat{\mathbf{n}}_\perp \cdot \mathcal{R}_S \cdot \hat{\mathbf{n}}_\perp$. The resonance appears for $b \gtrsim 0.1$ in the stationary transport, which is satisfied in the Coulomb-blockade regime. There the spin decay is limited by next-to-leading order processes (cotunneling) with rate $\Gamma_{\perp,\parallel} \sim \Gamma^2/U$, which can indeed be made smaller by reducing the tunnel couplings than the spin-precession frequency $B_\perp \sim \Gamma$ at resonance. The strongest contrast in the stability diagram is expected for $b \approx 1$ when roughly half a spin revolution happens within the electron dwell time in the QD. By contrast, in the limit $b \gg 1$, the spin coherence lasts much longer than one spin revolution and underdamped spin-precession cycles becomes feasible. The underdamped spin precession leads to no qualitative modifications of the resonance in the stationary conductance, but can nevertheless be probed experimentally by a simple gate-pulsing scheme. In the latter, the precession axis is controlled by electrical means and the rotation angle by the duration of the pulses. This allows one to determine the magnitude of the exchange field and

in combination with stationary-conductance measurements to determine the anisotropy of the spin decay all electrically. This can even be used to realize every single-spin qubit gate operation in an all-electric way.

Besides opening new avenues for spintronics and single-spin control, the spin resonance studied here provides an illustration of a generic concept in the simplest conceivable setting: such an anomalous resonance can appear in any open quantum system with quasidegenerate states whose coherence is described by a Bloch vector. For a two-level system, it is required that (i) the Bloch vector suffers only from little decoherence, (ii) the coherent evolution is dominated by a renormalization-induced field vector—because of level degeneracy—and (iii) which is induced by an environment that breaks symmetries (which are often present in idealized models). When such a system is tuned by experimentally accessible parameters, a resonance unrelated to any energy splitting can appear when the field vector becomes perpendicular to the Bloch vector.

This can be extended to N -fold degenerate multiplets, described by a generalized Bloch vector and an associated renormalization field vector. Interestingly, in this case the precession takes place in a higher dimensional space and is expected to be overlooked even more easily as compared to the simple case studied here. Scenarios can be envisaged in nuclear spin systems [67], double QDs [68], or vibrating molecular devices [53,69,70]. Our simple example shows that, interestingly, Coulomb interactions realize both requirements (i) and (ii) while noncollinear spin valves naturally provide (iii).

ACKNOWLEDGMENTS

We acknowledge discussions with M. Baumgärtel, S. Das, S. Herzog, M. Misiorny, and F. Reckermann, and financial support of the Swiss National Science Foundation via the NCCR QSIT (B.S.), and the Swedish Research Council (VR) (M.L.).

APPENDIX A: QUANTUM MASTER EQUATIONS AND PAULI SUPERBASIS

In this Appendix we outline how our coupled differential equations for operator averages (13) can be obtained from the general kinetic equation (12) for the reduced operator of the QD. For this purpose, we use a Liouville-space notation whose key elements we briefly review.

Applying the real-time diagrammatic technique [52,54], one can express the kinetic equation of the reduced density operator $\rho(t)$ of the QD as

$$|\dot{\rho}(t)\rangle = -iL|\rho(t)\rangle + \int_{-\infty}^t dt' W(t-t')|\rho(t')\rangle. \quad (\text{A1})$$

Here we introduced a bra-ket notation for linear operators $|A\rangle : \mathcal{H} \rightarrow \mathcal{H}$ acting on a Hilbert space \mathcal{H} , which altogether form the Liouville space \mathcal{L} . Furthermore, L and W denote *superoperators*, which are operators $\mathcal{S} : \mathcal{L} \rightarrow \mathcal{L}$ mapping a Liouville-space element on another Liouville-space element. In particular, $L\bullet = [H, \bullet]$ mediates the internal evolution of the density operator by the QD Hamiltonian H , where the dot “ \bullet ”

denotes the operator that L acts on. Furthermore, $W(t - t')$ is the real-time diagrammatic kernel that incorporates the effect of the environment on the evolution of the reduced system. We next carry out a Markov approximation, that is, we replace $|\rho\rangle(t') \approx |\rho\rangle(t)$ in Eq. (A1) and obtain

$$|\dot{\rho}(t)\rangle = [-iL + W]|\rho(t)\rangle. \quad (\text{A2})$$

Here $W = \int_0^\infty dt e^{izt} W(t)|_{z=i0}$ is the zero-frequency component of the kernel. One can prove [52,54] that the stationary state calculated from Eq. (A2) is the *exact* stationary solution of Eq. (A1). For actual calculations, Eqs. (A1) and (A2) are expressed in terms of matrix elements. To achieve this goal, one introduces the following scalar product in Liouville space [71]:

$$(A|B) := \text{Tr}(A^\dagger B). \quad (\text{A3})$$

An orthonormal *superbasis* is a set of superstates $\{|A\rangle\}$ that is orthonormal with respect to this scalar product,

$$(A|B) = \delta_{AB}, \quad (\text{A4})$$

and satisfies the completeness relation:

$$\mathcal{I} = \sum_A |A\rangle\langle A|. \quad (\text{A5})$$

Here \mathcal{I} denotes the superidentity $\mathcal{I}|A\rangle = |A\rangle$ for any $|A\rangle$. As a consequence, any superstate $|O\rangle$ can be expanded into such an orthonormal basis by $|O\rangle = \sum_A O_A |A\rangle$ with coefficients $O_A = (A|O)$ and any superoperator can be expressed as $\mathcal{S} = \sum_{A,B} \mathcal{S}_{AB} |A\rangle\langle B|$ with $\mathcal{S}_{AB} = (A|[\mathcal{S}|B])$. Usually, Eq. (A2) is expressed in terms of matrix elements for the superbasis $|a,b\rangle := |a\rangle\langle b|$, which yields

$$\dot{\rho}_{ab} = -iL_{a'b'}^{ab}\rho_{a'b'} + W_{a'b'}^{ab}\rho_{a'b'}, \quad (\text{A6})$$

with $\rho_{ab} = (a,b|\rho) = \text{Tr}(|a\rangle\langle b|^\dagger \rho)$ and $\mathcal{S}_{a'b'}^{ab} = (a,b|\mathcal{S}|a',b') = \text{Tr}(|a\rangle\langle b|^\dagger [\mathcal{S}|a'\rangle\langle b'|])$ for $\mathcal{S} = L, W$. In the Keldysh-contour formulation of real-time diagrammatics [72,73], diagram rules are given for the kernel matrix elements $W_{a'b'}^{ab}$. The diagonal matrix elements ρ_{aa} are interpreted as occupation probabilities and the off-diagonal elements ρ_{ab} as coherences. For a different choice of the basis states, however, the coherences in the former basis contribute to the occupation probabilities in the new basis. Thus, the interpretation as “probabilities” and “coherences” is meaningful only if a specific basis is singled out by the symmetry of the problem. For the single-level Anderson model we consider here, this would be the case for nonmagnetic electrodes. In this case, one can start from the Hilbert space basis $\{|0\rangle, |\uparrow\rangle, |\downarrow\rangle, |2\rangle\}$ with a fixed quantization axis for the spin. All coherences between spin states are zero in the stationary limit.

For noncollinear lead polarizations, such a spin quantization axis does not exist, cf. Sec. II A. Thus, it is helpful to expand Eq. (A2) in terms of different supermatrix elements such that all expressions are independent of the quantization axis. For this purpose, we chose a superbasis $\{|A\rangle\}$ consisting of *observables*. The reduced density matrix can then be expanded as

$$|\rho\rangle = \sum_A A|A\rangle, \quad (\text{A7})$$

where

$$A = (A|\rho) = \text{Tr}(A\rho) \quad (\text{A8})$$

is the expectation value of observable $A(=A^\dagger)$ —an object with an intuitive physical interpretation in contrast to the matrix elements ρ_{ab} .

For the single-level Anderson model, a suitable superbasis is the *Pauli superbasis*. We focus here on the charge-conserving setup without superconductor (see Fig. 1). For the nondegenerate subspaces with zero ($n=0$) and two ($n=2$) electrons, these are simply the projectors

$$|\check{r}_0^0\rangle := \hat{P}_0 = |0\rangle\langle 0| \quad (\text{A9})$$

and

$$|\check{r}_0^2\rangle := \hat{P}_2 = |2\rangle\langle 2|. \quad (\text{A10})$$

For the subspace of charge state $n=1$, we introduce

$$|\check{r}_\mu^1\rangle := \sum_{\sigma\sigma'} (\check{r}_\mu)_{\sigma\sigma'} |\sigma\rangle\langle\sigma'|, \quad (\text{A11})$$

where $\mu = 0, 1, 2, 3$, $(\check{r}_0)_{\sigma\sigma'} = \delta_{\sigma\sigma'}/\sqrt{2}$, and $(\check{r}_{\mu=i})_{\sigma\sigma'} = (\sigma_i)_{\sigma\sigma'}/\sqrt{2}$ involving the Pauli matrices σ_i for $i = 1, 2, 3$. The element $|\check{r}_0^1\rangle = \hat{P}_1/\sqrt{2}$ is proportional to the scalar projection operator on charge state 1 and the elements $|\check{r}_i^1\rangle = \sqrt{2}\hat{S}_i$ are proportional to the vector components of the spin operator. Altogether, these six superstates provide an orthonormal basis for the subspace of the charge-diagonal QD operators,

$$(\check{r}_\mu^n | \check{r}_{\mu'}^{n'}) = \delta^{nn'} \delta_{\mu\mu'}, \quad (\text{A12})$$

$$\mathcal{I}_C = \sum_{n\mu} |\check{r}_\mu^n\rangle\langle\check{r}_\mu^n|, \quad (\text{A13})$$

where \mathcal{I}_C denotes the identity operator in the subspace of charge-diagonal operators. The factors $1/\sqrt{2}$ are introduced in the definition of $(\check{r}_\mu)_{\sigma\sigma'}$ to avoid additional factors in Eqs. (A12) and (A13). The Pauli superbasis is sufficient to expand the density operator $|\rho\rangle$ [74], which reads by applying Eq. (A7):

$$|\rho\rangle = \frac{1}{\sqrt{2}} \sum_n p_n |\check{r}_0^n\rangle + \sqrt{2} \mathbf{S} \cdot |\check{\mathbf{r}}^1\rangle, \quad (\text{A14})$$

where $p_1 = \sqrt{2} \text{Tr}(\check{r}_0^1 \rho)$, $p_{0/2} = \text{Tr}(\check{r}_0^{0/2} \rho)$ are the occupation probabilities of charge state n and $\mathbf{S} = \text{Tr}(\check{\mathbf{r}}^1 \rho)/\sqrt{2}$ is the average spin operator (4). Importantly, Eq. (A14) is *covariant*, i.e., form invariant under a change of the spin-quantization axis or the real-space coordinate system. This also illustrates that working in Liouville space does not only give more compact expressions but it also results in a physically more transparent description of the QD state and its dynamics.

APPENDIX B: KINETIC EQUATIONS AND CURRENT FOR QUANTUM-DOT SPIN VALVE

1. Rates for kinetic equations and current

In this Appendix we give all expressions for the rates in the kinetic equations (13), which read

$$\begin{aligned} \dot{p}_0 &= -2\Gamma_0 p_0 + \Gamma_1 p_1 + 2\mathbf{G}_{pS} \cdot \mathbf{S}, \\ \dot{\mathbf{S}} &= +\mathbf{G}_{Sp}^0 p_0 - \frac{1}{2} \mathbf{G}_{Sp}^1 p_1 - \mathcal{R}_S \cdot \mathbf{S} - \mathbf{B} \times \mathbf{S}. \end{aligned} \quad (\text{B1})$$

The charge-relaxation rates are given by

$$\Gamma^{0/1} = \Gamma_0^\pm \pm \text{Im} \left(K_{00}^+ + \frac{1}{2} \sum_\rho K_{\rho\rho}^- \right), \quad (\text{B2})$$

where Greek indices take the values $\rho = 0, 1, 2, 3$ and Latin indices take the values $i = 1, 2, 3$. Furthermore, the vectorial spin-to-charge conversion rates are given by

$$(G_{ps})_i = \Gamma_i^- - \text{Im} \left(K_{i0}^+ + \frac{1}{2} K_{i0}^- + \frac{1}{2} K_{0i}^- \right) - \frac{1}{2} \sum_{jk} \varepsilon_{ijk} \text{Re}(K_{jk}^-), \quad (\text{B3})$$

the vectorial charge-to-spin conversion rates are given by

$$(G_{Sp}^{0/1})_i = \Gamma_i^\pm \pm \text{Im} \left(K_{i0}^+ + \frac{1}{2} K_{i0}^- + \frac{1}{2} K_{0i}^- \right) \mp \frac{1}{2} \sum_{jk} \varepsilon_{ijk} \text{Re}(K_{jk}^-), \quad (\text{B4})$$

the symmetric spin-decay tensor is defined by

$$(\mathcal{R}_S)_{ij} = \delta_{ij} \Gamma_0^- + \delta_{ij} \text{Im} \left(-\frac{1}{2} K_{00}^- + \frac{1}{2} \sum_i K_{ii}^- - D_{00}^{+-} \right) - \frac{1}{2} \text{Im}(K_{ij}^- + K_{ji}^- + X_{ij}^{+-} + X_{ji}^{+-}), \quad (\text{B5})$$

and, finally, the vectorial exchange field reads

$$B_i = \beta_i + \text{Re} \left(\frac{1}{2} K_{i0}^- - \frac{1}{2} K_{0i}^- + D_{i0}^{+-} \right). \quad (\text{B6})$$

The above rates first contain terms of $O(\Gamma)$, $\Gamma_\rho^X(\varepsilon) = \sum_r \Gamma_{r,\rho}^X(\varepsilon)$ and $\beta_\rho(\varepsilon) = \sum_r \beta_{r,\rho}(\varepsilon)$, with

$$\Gamma_{r,\rho=0}^X(\varepsilon) = \Gamma_r^X(\varepsilon) = 2\pi |t_r|^2 \bar{v}_r f[\chi(\varepsilon - \mu_r)/T], \quad (\text{B7})$$

$$\Gamma_{r,\rho=i}^X(\varepsilon) = \Gamma_r^X(\varepsilon) n_{r,i} \quad (i = 1, 2, 3), \quad (\text{B8})$$

$$\beta_{r,\rho}(\varepsilon) = P \int_{-W}^{+W} \frac{d\omega}{\pi} \frac{\Gamma_{r,\rho}^+(\omega)}{\varepsilon - \omega}, \quad (\text{B9})$$

with P denoting the principal value integral and the Fermi function $f(x) = 1/(e^x + 1)$. Here the spatial components $\rho = 1, 2, 3$ point along by the polarization vector \mathbf{n}_r of lead r . Furthermore, the $O(\Gamma^2)$ contributions incorporate two different tensors, namely

$$X_{\rho_2\rho_1}^{\chi_2\chi_1} = \int_{-W}^{+W} \int_{-W}^{+W} \frac{d\omega_1}{\pi} \frac{d\omega_2}{\pi} \Gamma_{\rho_2}^{\chi_2}(\omega_2) \Gamma_{\rho_1}^{\chi_1}(\omega_1) \times \frac{1}{i0 + \omega_2 - \varepsilon} \frac{1}{i0 + \omega_2 - \omega_1} \frac{1}{i0 - \omega_1 + \varepsilon}, \quad (\text{B10})$$

and $D_{\rho_2\rho_1}^{\chi_2\chi_1}$ given by the same expression when replacing the rightmost denominator in the above expression by $1/[i0 + \omega_2 - \varepsilon]$. In contrast to previous works, we evaluate the full complex integral to completely capture the dynamics of the spin coherences in the Coulomb blockade regime to order Γ^2 .

Adding the X and D integrals, we obtain the simpler function

$$K_{\rho_2\rho_1}^{\chi_1} = \bar{\chi}_2 (X_{\rho_2\rho_1}^{\chi_2\chi_1} + D_{\rho_2\rho_1}^{\chi_2\chi_1}) = [\chi_1 \beta'_{\rho_2} \beta_{\rho_1} + \Gamma'_{\rho_2} \Gamma_{\rho_1}^{\chi_1}] + i[\chi_1 \Gamma'_{\rho_2} \beta_{\rho_1} - \beta'_{\rho_2} \Gamma_{\rho_1}^{\chi_1}], \quad (\text{B11})$$

where $\Gamma'_\rho = d\Gamma_\rho^+/d\varepsilon$ and $\beta'_\rho = d\beta_\rho/d\varepsilon$.

We note that the leading-order Γ contribution to the spin-relaxation tensor (B5) is isotropic while the next-to-leading order Γ^2 contribution renders the spin decay anisotropic. Since the leading-order term is suppressed in the Coulomb-blockade regime, the spin decay can indeed become significantly anisotropic. In contrast to the decay rates, the first-order Γ contribution to the exchange field (B9) is only logarithmically suppressed.

The expression for the average current from lead r into the QD reads

$$I_r = 2\Gamma_{r,0} p_0 - \Gamma_{r,1} p_1 - 2\mathbf{G}_{r,pS} \cdot \mathbf{S}, \quad (\text{B12})$$

with

$$\Gamma_{r,0/1} = \Gamma_r^\pm \pm \text{Im} \left(K_{r,00}^+ + \frac{1}{2} \sum_\rho K_{r,\rho\rho}^- \right), \quad (\text{B13})$$

$$(G_{r,pS})_i = \Gamma_{r,i}^- - \text{Im} \left(K_{r,i0}^+ + \frac{1}{2} K_{r,i0}^- + \frac{1}{2} K_{0i}^- \right) + \text{Im} (X_{r,0i}^{+-} - X_{r,i0}^{+-}) - \frac{1}{2} \sum_{\rho_2\rho_1} \varepsilon_{i\rho_2\rho_1} \text{Re} (K_{r,\rho_2\rho_1}^-), \quad (\text{B14})$$

where $X_{r,\rho_2\rho_1}^{\chi_2\chi_1}$ is obtained from Eq. (B10) by replacing $\Gamma_{\rho_2}^{\chi_2}(\omega_2) \rightarrow \Gamma_{r,\rho_2}^{\chi_2}(\omega_2)$ and $K_{r,\rho_2\rho_1}^X$ is obtained from Eq. (B12) by replacing $\beta'_{\rho_2} \rightarrow \beta'_{r,\rho_2}$ and $\Gamma'_{\rho_2} \rightarrow \Gamma'_{r,\rho_2}$, respectively.

The X -type integrals, Eq. (B10), and the corresponding D -type integrals are computed numerically as we explain next. We convert the double frequency integral into a double summation over Matsubara frequencies by first substituting $x_2 = \omega_2/T$ and $x_1 = -\omega_2/T$ and splitting the Fermi functions $f(xT) = g^+(x) + g^-(x)$ into their symmetric part $g^+(x) = 1/2$ and their antisymmetric part $g^-(x) = -\tanh(x/2)/2$, respectively. We then integrate over x_1 and x_2 using complex integration, closing the integration contour in the upper half of the complex plane. By virtue of the residue theorem, one can derive the following relation for the generic type of integrals occurring after these manipulations:

$$\begin{aligned} & \int_{-R}^{+R} dx_1 \int_{-R}^{+R} dx_2 g^{q_1}(x_1) g^{q_2}(x_2) \\ & \times \frac{1}{x_j - \lambda_2 + i0} \frac{1}{x_1 + x_2 + i0} \frac{1}{x_1 - \lambda_1 + i0} \\ & = -4\pi^2 \delta_{q_1,-} \delta_{q_2,-} \sum_{k_1,k_2}^{k_R} \frac{1}{z_{kj} - \lambda_2} \frac{1}{z_{k1} + z_{k2}} \frac{1}{z_{k1} - \lambda_1} \\ & + 2\pi i \delta_{q_1,-} \delta_{j,1} \sum_{k_1}^{k_R} \frac{1}{z_{k1} - \lambda_2} \frac{1}{z_{k1} - \lambda_1} \sum_{k_2}^{k_R} M_{k_2}^{q_2} \\ & + O\left(\frac{1}{R}\right), \end{aligned} \quad (\text{B15})$$

where $j = 1, 2$, $q_1, q_2 = \pm$, $z_{k_{1,2}} = i\pi(2k_{1,2} + 1)$ are the Matsubara frequencies, and $0 \leq k \leq k_R = \lceil \frac{R}{2\pi} - \frac{1}{2} \rceil$ with $\lceil x \rceil$ denoting the smallest integer that is not less than x . We additionally used the abbreviation

$$M_{k_2}^{q_2} = \frac{1}{2} \left[q_2 \ln \left(\frac{z_{k_2} + iR}{z_{k_2} + R} \right) + \ln \left(\frac{z_{k_2} - R}{z_{k_2} + iR} \right) \right]. \quad (\text{B16})$$

The above double Matsubara sums are then evaluated numerically.

2. Extension of former studies

In this Appendix, we compare our kinetic equations (13) to those of prior studies of QD spin valves and results from other approaches: In fact, our theoretical approach presents a technical step forward relative to the previous works, which is a reason why the spin resonance has been overlooked for a long time.

Quantum master equations. First, the lowest-order Γ contribution to our equations complies with the results given in Refs. [36,40] taking the limit $U \rightarrow \infty$. However, a lowest-order expansion in Γ is not sufficient in the Coulomb blockade regime since these terms are exponentially suppressed with the distance $|\varepsilon - \mu_r|/T$ from the Fermi levels. By contrast, some $O(\Gamma^2)$ terms are only algebraically suppressed and therefore dominate there. In particular, this is associated with a spin decay due to cotunneling that could obliterate the coherent spin-precession features. This was noted in Ref. [26] where the spin resonance was reported to emerge on the flank of the Coulomb diamond using an $O(\Gamma)$ kinetic equation, but could not be reliably followed into the Coulomb blockade regime. However, the sharp resonance feature we find here even when $O(\Gamma^2)$ cotunneling corrections are included shows that spin-precession effects can still be dominant—as anticipated in the introduction from time-scale estimations.

Next-to-leading order corrections $\sim \Gamma^2$ have been included in other studies of the same model, for example, in Refs. [24,28,76]; however these works address only *collinearly* polarized ferromagnets. Here the spin precession cannot occur since the spin accumulation and the exchange field are collinear (cf. the expressions of the rates in Appendix B 1). In Ref. [77], also the noncollinear magnetic configuration is studied, but the QD is assumed to be deposited on a ferromagnetic substrate causing a large splitting $\varepsilon_\uparrow - \varepsilon_\downarrow \gg \Gamma$ of the two spin states as compared to the tunnel coupling, so that the spin components transverse to this splitting field have negligible impact.

The difficult case of degenerate QD spin states, noncollinear polarizations, and cotunneling corrections has to our knowledge been addressed only in Ref. [50]. While the kinetic equations given there include all the terms that correspond to the imaginary parts up to $O(\Gamma^2)$ and the real parts up to $O(\Gamma)$ in the rates (B2)–(B6), our equations additionally include the $O(\Gamma^2)$ corrections to the real parts of these rates. This is done via the Matsubara double summation (B15), which is implemented numerically. For other models with higher degree of symmetry, which only require the imaginary part of these integrals, this can be avoided (see Ref. [52]). Thus, we include, for example, in the exchange field (B6) *all renormalization effects* up to $O(\Gamma^2)$. Our results actually

confirm that the $O(\Gamma^2)$ corrections to the exchange field are not important near the particle-hole symmetry point, at least for an accurate prediction of the resonance position. However, this is not clear from the start and required a careful numerical examination. Furthermore, our kinetic equations (13) are compactly expressed in equations for physically meaningful observable averages.

Other methods. Several other works dealing with noncollinearly polarized leads employ completely different techniques, such as a Green's function approach in the noninteracting approximation [25], in a Hartree-Fock approximation [21,22,51], or restricted to zero bias [23]. As these works do not employ kinetic equations, a direct comparison of the results is more difficult. Some of these studies address different exchange field effects also for noncollinear polarizations [23,51]; yet, a sharp resonance has not been reported there.

Thus, even though we investigate in this paper the well-studied Anderson QD model with noncollinear ferromagnets, our technically advanced analysis gives us access to a parameter regime for which reliable predictions were hardly possible before. This allows us to go beyond previous works. The reason that our spin resonance without spin splitting has been overlooked so far is that it requires the careful treatment of the combination of (i) slow decoherence of the spin in the Coulomb blockade regime, (ii) the degeneracy of the spin levels allowing the coherent evolution to be dominated by the exchange field, and (iii) complete rotational symmetry breaking by noncollinearly polarized ferromagnet.

3. Solving the quantum master equation in the Coulomb blockade regime

As explained in Sec. II B, in the Coulomb blockade regime the next-to-leading order Γ^2 contributions can dominate over the leading-order Γ contributions. This also requires careful consideration when solving Eq. (13) for the occupation probabilities p_n and the average spin \mathbf{S} : To solve the kinetic equations one could perform a systematic perturbation expansion not only for the kernels but also for the probabilities $p_n = p_n^{(0)} + p_n^{(1)} + \dots$ and the spin $\mathbf{S} = \mathbf{S}^{(0)} + \mathbf{S}^{(1)} + \dots$ in orders of Γ , and solve Eq. (12) then order by order in Γ . This has the advantage that the current is evaluated consistently to a given order in Γ . This procedure works well as long as lowest-order Γ tunneling processes (sequential tunneling) are present but fails in the Coulomb blockade regime where sequential tunneling is exponentially suppressed and cotunneling dominates. This is particularly important for the results obtained for infinite U , shown in Fig. 10. Therefore, we use an alternative procedure in which only the kernels (but not the probabilities and the spin) are expanded in powers of Γ . It is, thus, the *kernels* that are to be consistently evaluated to a given order in Γ : not the density operator or observables such as the current. This issue has been thoroughly discussed elsewhere for our model [24] but also in a more general context [52] including, e.g., vibrational degrees of freedom on the QD. Although the current we obtain may comprise terms of order Γ^3 , we checked that the spin resonance is clearly not an artifact of those terms. By varying Γ , the resonance current is found to scale maximally as Γ^2 or a lower power but not as Γ^3 .

4. Incorporation of superconducting terminal

We comment here on the results that we show in Fig. 6 when adding a proximal superconductor to the setup. To simplify the analytical calculations (which are already quite involved without a superconductor), we included here only the leading-order Γ contribution in the tunneling rates. Consistent with this, the charging energy U has been chosen of moderate size there. There are several reasons why this simplification does not affect the conclusions we draw from Fig. 6 that concern only the resonance *position*. First, we note that the effect of the superconductor is clearly visible when moving into the Coulomb diamond but still within the thermal broadening window of $4T$ around the single-electron tunneling resonances in Fig. 6. Here a leading-order Γ calculation gives reliable predictions without any question. Second, we note that this regime covers quite a large part of Fig. 6 since the presence of the superconductor reduces the size of the effective Coulomb diamond in the stability diagram, as one sees from comparing Figs. 2 and 6. The exponential suppression of the $O(\Gamma)$ rates is thus attenuated, but it may still be strong near the particle-hole symmetry point. Here one should in principle include $O(\Gamma^2)$ corrections. However, and this is our third point, by comparing results of $O(\Gamma)$ (not shown here), and $O(\Gamma^2)$ (Fig. 2) for the same parameters without superconductor, we know that the resonance is not diminished, as clearly demonstrated by Fig. 2, but only slightly broadened due to the additional spin decay introduced by cotunneling (cf. Sec. III F). Once the resonance appears, its position is determined by the *first-order* exchange field (cf. Sec. III A), modified by the proximal superconductor (cf. Sec. III D), the effect we wished to illustrate here. The cotunneling corrections are not needed to draw a conclusion about the resonance *position*.

5. Non-Markovian corrections

Finally, we comment on the validity of the Markovian approximation underlying our kinetic equations (13) for our study of the time-dependent pulsing scheme. To study time-dependent problems in the Coulomb blockade regime, one must in principle also include non-Markovian corrections into the kernel [78]. However, non-Markovian corrections appear only as modifications of the *next-to-leading order* contributions. Thus, non-Markovian corrections do not affect the exchange field, which is dominated by leading-order terms and determines the position of the spin resonance and the frequency of the spin precession. On the contrary, the corrections do alter the spin-decay tensor \mathcal{R}_S and thereby the time constant of the damped spin oscillations. In spite of this, the latter will still be of $O(\Gamma^2/U)$ in the Coulomb blockade regime, which we have identified as the crucial requirement for the underdamped spin precession. Including non-Markovian

corrections is, hence, required only for a quantitative analysis but not to demonstrate the viability of an underdamped spin precession, which is our aim here. It should be noted that if such accuracy is desirable, other spin-decay mechanisms should also be taken into account (see Sec. IV C), which is clearly beyond the scope of this work.

APPENDIX C: PARTICLE-HOLE SYMMETRY

In Sec. III C our discussion of the resonance position applied only to the left half of the Coulomb diamond, i.e., for gate voltages $\delta = U + 2\varepsilon > 0$; cf. Fig. 2. Here we show that the resonance extends point symmetrically with respect to the particle-hole symmetry point $(\delta, V_b) = (0, 0)$. In the region to the right of this point, where $\delta < 0$, the resonance condition requires the exchange field to be perpendicular to the *drain* polarization:

$$\mathbf{B} \cdot \hat{\mathbf{n}}_d = 0 \quad (\delta < 0). \quad (\text{C1})$$

This condition is fulfilled for *negative* resonant bias $V_b^* < 0$. Thus, the drain refers here to the same physical electrode as the source in Eq. (15) because changing the sign of the bias exchanges the role of source and drain.

Equation (C1) can be understood physically as follows: For $\delta < 0$, the electrochemical potential of the leads is closer to that for the doubly occupied QD and therefore the current predominantly involves the doubly occupied QD state. Consequently, when an electron leaves the QD, it leaves behind a *hole* polarized along $\hat{\mathbf{n}}_d$. However, an accumulation of hole spins can be efficiently prevented by the exchange field \mathbf{B} if the latter is directed perpendicular to $\hat{\mathbf{n}}_d$, that is, if condition (C1) is fulfilled.

In analogy to Eq. (19), condition (C1) can be recast as

$$\frac{a'}{q'} = 1, \quad (\text{C2})$$

with

$$a' = \frac{\Gamma_s n_s \cos(\alpha)}{\Gamma_d n_d}, \quad (\text{C3})$$

and

$$q' := \frac{\phi_d(\varepsilon) - \phi_d(\varepsilon + U)}{\phi_s(\varepsilon) - \phi_s(\varepsilon + U)} \quad (\delta < 0), \quad (\text{C4})$$

where the spin injection asymmetry ratio a' is defined differently as in Eq. (19). Equation (C2) complies with Eq. (19): Mapping $(\delta, V_b) \rightarrow (-\delta, -V_b)$, we have to replace $q \rightarrow 1/q'$ and $a \rightarrow 1/a'$ since the roles of source and drain are interchanged. It is therefore sufficient to discuss only the case $\delta > 0$ as we did in Sec. III C as all results hold for $\delta < 0$ accordingly by reversing the signs of δ and V_b .

-
- [1] S. Loth, K. von Bergmann, M. Ternes, A. F. Otte, C. Lutz, and A. Heinrich, *Nat. Phys.* **6**, 340 (2010).
 [2] L. Besombes, C. L. Cao, S. Jamet, H. Boukari, and J. Fernández-Rossier, *Phys. Rev. B* **86**, 165306 (2012).

- [3] A. A. Khajetoorians, B. Baxevanis, C. Hübner, T. Schlenk, S. Krause, T. O. Wehling, S. Lounis, A. Lichtenstein, D. Pfannkuche, J. Wiebe, and R. Wiesendanger, *Science* **339**, 55 (2013).

- [4] J. R. Petta, A. C. Johnson, J. M. Taylor, E. A. Laird, A. Yacoby, M. D. Lukin, C. M. Marcus, M. P. Hanson, and A. C. Gossard, *Science* **309**, 2180 (2005).
- [5] F. H. L. Koppens, C. Buizert, K. J. Tielrooij, I. T. Vink, K. C. Nowack, T. Meunier, L. P. Kouwenhoven, and L. M. K. Vandersypen, *Nature (London)* **442**, 766 (2006).
- [6] K. C. Nowack, F. H. L. Koppens, Y. V. Nazarov, and L. M. K. Vandersypen, *Science* **318**, 1430 (2007).
- [7] H. Bluhm, S. Foletti, I. Neder, M. Rudner, D. Mahalu, V. Umansky, and A. Yacoby, *Nat. Phys.* **7**, 109 (2010).
- [8] J. Fernández-Rossier and R. Aguado, *Phys. Rev. Lett.* **98**, 106805 (2007).
- [9] L. Bogani and W. Wernsdorfer, *Nat. Mater.* **7**, 179 (2008).
- [10] A. S. Zyazin, J. W. van den Berg, E. A. Osorio, H. S. van der Zant, N. P. Konstantinidis, F. May, M. Leijnse, W. Hofstetter, M. R. Wegewijs, C. Danieli, and A. Cornia, *Nano Lett.* **10**, 3307 (2010).
- [11] M. Urdampilleta, S. Klyatskaya, J.-P. Cleuziou, M. Ruben, and W. Wernsdorfer, *Nat. Mater.* **10**, 502 (2011).
- [12] A. J. Heinrich, J. A. Gupta, C. P. Lutz, and D. M. Eigler, *Science* **306**, 466 (2004).
- [13] S. Kahle, Z. Deng, N. Malinowski, C. Tonnoir, A. Forment-Aliaga, N. Thontasen, G. Rinke, D. Le, V. Turkowski, T. S. Rahman *et al.*, *Nano Lett.* **12**, 518 (2012).
- [14] B. W. Heinrich, L. Braun, J. I. Pascual, and K. J. Franke, *Nat. Phys.* **9**, 765 (2013).
- [15] M. Julliere, *Phys. Lett. A* **54**, 225 (1975).
- [16] M. N. Baibich, J. M. Broto, A. Fert, F. Nguyen Van Dau, F. Petroff, P. Etienne, G. Creuzet, A. Friederich, and J. Chazelas, *Phys. Rev. Lett.* **61**, 2472 (1988).
- [17] G. Binasch, P. Grünberg, F. Saurenbach, and W. Zinn, *Phys. Rev. B* **39**, 4828 (1989).
- [18] R. E. Camley and J. Barnaś, *Phys. Rev. Lett.* **63**, 664 (1989).
- [19] J. C. Slonczewski, *Phys. Rev. B* **39**, 6995 (1989).
- [20] P. Seneor, A. Bernand-Mantel, and F. Petroff, *J. Phys. Condens. Matter* **19**, 165222 (2007).
- [21] N. Sergueev, Q. F. Sun, H. Guo, B. G. Wang, and J. Wang, *Phys. Rev. B* **65**, 165303 (2002).
- [22] M. Wilczyński, R. Świrkowicz, W. Rudziński, J. Barnaś, and V. Dugaev, *J. Magn. Magn. Mater.* **290–291**, 209 (2005).
- [23] J. Fransson, *Europhys. Lett.* **70**, 796 (2005).
- [24] I. Weymann, J. König, J. Martinek, J. Barnaś, and G. Schön, *Phys. Rev. B* **72**, 115334 (2005).
- [25] J. N. Pedersen, J. Q. Thomassen, and K. Flensberg, *Phys. Rev. B* **72**, 045341 (2005).
- [26] M. M. E. Baumgärtel, M. Hell, S. Das, and M. R. Wegewijs, *Phys. Rev. Lett.* **107**, 087202 (2011).
- [27] G. Usaj and H. U. Baranger, *Phys. Rev. B* **63**, 184418 (2001).
- [28] I. Weymann, J. Barnaś, J. König, J. Martinek, and G. Schön, *Phys. Rev. B* **72**, 113301 (2005).
- [29] D. M. Zumbühl, C. M. Marcus, M. P. Hanson, and A. C. Gossard, *Phys. Rev. Lett.* **93**, 256801 (2004).
- [30] J. Paaske, A. Rosch, P. Wölffe, N. Mason, C. M. Marcus, and J. Nygård, *Nat. Phys.* **2**, 460 (2006).
- [31] G. Kiršanskas, J. Paaske, and K. Flensberg, *Phys. Rev. B* **86**, 075452 (2012).
- [32] A. N. Pasupathy, R. C. Bialczak, J. Martinek, J. E. Grose, L. A. K. Donev, P. L. McEuen, and D. C. Ralph, *Science* **306**, 86 (2004).
- [33] K. Hamaya, M. Kitabatake, K. Shibata, M. Jung, M. Kawamura, K. Hirakawa, T. Machida, T. Taniyama, S. Ishida, and Y. Arakawa, *Appl. Phys. Lett.* **91**, 232105 (2007).
- [34] J. R. Hauptmann, J. Paaske, and P. E. Lindelof, *Nat. Phys.* **4**, 373 (2008).
- [35] M. Gaass, A. K. Hüttel, K. Kang, I. Weymann, J. von Delft, and C. Strunk, *Phys. Rev. Lett.* **107**, 176808 (2011).
- [36] J. König and J. Martinek, *Phys. Rev. Lett.* **90**, 166602 (2003).
- [37] J. Martinek, M. Sindel, L. Borda, J. Barnaś, J. König, G. Schön, and J. von Delft, *Phys. Rev. Lett.* **91**, 247202 (2003).
- [38] J. König, J. Martinek, J. Barnaś, and G. Schön, in *CFN Lectures on Functional Nanostructures*, edited by K. Busch *et al.*, Lecture Notes in Physics (Springer, Berlin, 2005), p. 145.
- [39] M.-S. Choi, D. Sánchez, and R. López, *Phys. Rev. Lett.* **92**, 056601 (2004).
- [40] M. Braun, J. König, and J. Martinek, *Phys. Rev. B* **70**, 195345 (2004).
- [41] J. Martinek, M. Sindel, L. Borda, J. Barnaś, R. Bulla, J. König, G. Schön, S. Maekawa, and J. von Delft, *Phys. Rev. B* **72**, 121302 (2005).
- [42] J. V. Holm, H. I. Jørgensen, K. Grove-Rasmussen, J. Paaske, K. Flensberg, and P. E. Lindelof, *Phys. Rev. B* **77**, 161406 (2008).
- [43] J. Splettstoesser, M. Governale, and J. König, *Phys. Rev. B* **86**, 035432 (2012).
- [44] S. Sobczyk, A. Donarini, and M. Grifoni, *Phys. Rev. B* **85**, 205408 (2012).
- [45] M. Misiorny, M. Hell, and M. R. Wegewijs, *Nat. Phys.* **9**, 801 (2013).
- [46] M. Braun, J. König, and J. Martinek, *Europhys. Lett.* **72**, 294 (2005).
- [47] M. Braun, J. König, and J. Martinek, *Phys. Rev. B* **74**, 075328 (2006).
- [48] B. Sothmann and J. König, *Phys. Rev. B* **82**, 245319 (2010).
- [49] B. Sothmann, D. Futterer, M. Governale, and J. König, *Phys. Rev. B* **82**, 094514 (2010).
- [50] I. Weymann and J. Barnaś, *Phys. Rev. B* **75**, 155308 (2007).
- [51] W. Rudziński, J. Barnaś, R. Świrkowicz, and M. Wilczyński, *Phys. Rev. B* **71**, 205307 (2005).
- [52] M. Leijnse and M. R. Wegewijs, *Phys. Rev. B* **78**, 235424 (2008).
- [53] S. Koller, M. Grifoni, M. Leijnse, and M. R. Wegewijs, *Phys. Rev. B* **82**, 235307 (2010).
- [54] H. Schoeller, *Eur. Phys. J. Special Topics* **168**, 179 (2009).
- [55] A. Martin-Rodero and A. Levy Yeyati, *Adv. Phys.* **60**, 899 (2011).
- [56] L. E. Hueso, J. M. Pruneda, V. Ferrari, G. Burnell, J. P. Valdés-Herrera, B. D. Simons, P. B. Littlewood, E. Artacho, A. Fert, and N. D. Mathur, *Nature (London)* **445**, 410 (2007).
- [57] A. V. Rozhkov and D. P. Arovas, *Phys. Rev. B* **62**, 6687 (2000).
- [58] S. De Franceschi, L. Kouwenhoven, C. Schönenberger, and W. Wernsdorfer, *Nat. Nanotechnol.* **5**, 703 (2010).
- [59] L. Hofstetter, A. Geresdi, M. Aagesen, J. Nygård, C. Schönenberger, and S. Csonka, *Phys. Rev. Lett.* **104**, 246804 (2010).
- [60] D. Futterer, J. Swiebodzinski, M. Governale, and J. König, *Phys. Rev. B* **87**, 014509 (2013).
- [61] J. Martinek, Y. Utsumi, H. Imamura, J. Barnaś, S. Maekawa, J. König, and G. Schön, *Phys. Rev. Lett.* **91**, 127203 (2003).
- [62] R. Hanson, L. P. Kouwenhoven, J. R. Petta, S. Tarucha, and L. M. Vandersypen, *Rev. Mod. Phys.* **79**, 1217 (2007).

- [63] T. Fujisawa, D. G. Austing, Y. Tokura, Y. Hirayama, and S. Tarucha, *J. Phys. Condens. Matter* **15**, R1395 (2003).
- [64] H. Schoeller, *Mesoscopic Electron Transport* (Kluwer, Amsterdam, 1997), p. 291.
- [65] F. H. L. Koppens, K. C. Nowack, and L. M. K. Vandersypen, *Phys. Rev. Lett.* **100**, 236802 (2008).
- [66] B. Sothmann, *Phys. Rev. B* **90**, 155315 (2014).
- [67] C. P. Slichter, *Principles of Magnetic Resonance* (Springer, Berlin, 1990), Vol. 1.
- [68] B. Wunsch, M. Braun, J. König, and D. Pfannkuche, *Phys. Rev. B* **72**, 205319 (2005).
- [69] A. Donarini, M. Grifoni, and K. Richter, *Phys. Rev. Lett.* **97**, 166801 (2006).
- [70] M. G. Schultz, *Phys. Rev. B* **82**, 155408 (2010).
- [71] H.-P. Breuer and F. Petruccione, *The Theory of Open Quantum Systems* (Oxford University Press, Oxford, 2002).
- [72] J. König, J. Schmid, H. Schoeller, and G. Schön, *Phys. Rev. B* **54**, 16820 (1996).
- [73] J. König, H. Schoeller, and G. Schön, *Phys. Rev. Lett.* **76**, 1715 (1996).
- [74] In principle, ten more superbasis elements have to be added to form a complete set of all superstates of the Liouville space of the QD, which has dimension $4^2 = 16$ because of the four-dimensional Hilbert space considered here. However, for expanding any observable or the density operator, eight of these superbasis elements are obsolete since they do not conserve the fermion parity [75]. Furthermore, we restrict our considerations here to the charge-conserving model without a superconductor.
- [75] R. B. Saptsov and M. R. Wegewijs, *Phys. Rev. B* **90**, 045407 (2014).
- [76] S. Koller, M. Grifoni, and J. Paaske, *Phys. Rev. B* **85**, 045313 (2012).
- [77] I. Weymann and J. Barnaś, *Eur. Phys. J. B* **46**, 289 (2005).
- [78] J. Splettstoesser, M. Governale, J. König, and M. Büttiker, *Phys. Rev. B* **81**, 165318 (2010).